1 **Title: Anatectic melt inclusions in ultra-high temperature granulites**

2 **Omar Gianola**[1], Omar Bartoli[1], Bernardo Cesare[1], Fabio Ferri[1], Andrea Galli[2], Silvio Ferrero[3],

3 Luca Capizzi[1,4], Christian Liebske[2], Laurent Remusat[5], Stefano Poli[6]

4 [1] Dipartimento di Geoscienze, Università degli Studi di Padova, Via G. Gradenigo 6, 35131 Padova,

5 Italy

6 [2] Institut für Geochemie und Petrologie, ETH Zürich, Switzerland

7 [3] Institut für Erd- und Umweltwissenschaften, Universität Potsdam, Potsdam, Germany

8 [4] Dipartimento di Scienze della Terra, Università degli Studi di Roma "La Sapienza", Roma, Italy

9 [5] Institut de Minéralogie, de Physique des Matériaux, et de Cosmochimie (IMPMC), UMR CNRS 7590

10 – Sorbonne Universités – UPMC – IRD – Muséum National d'Histoire Naturelle, Paris, France

11 [6] Dipartimento di Scienze della Terra "Ardito Desio", Università degli Studi di Milano, Milano, Italy

12

13 E-mail: omar.gianola@unipd.it

14

15 **Key words**: Fluid inclusions; Garnet; Granites; Gruf Complex; Nanogranitoids

16

17 **Abstract**

18 Partial melting up to ultra-high temperature (UHT) conditions is one of the major processes for

19 the geochemical differentiation and reworking of the mid- to lower continental crust, with

20 relevant implications on its rheological behaviour. UHT granulites from the Gruf Complex

21 (Central Alps) display garnet and sapphirine porphyroblasts containing a variety of primary

22 melt inclusions. Typically, melt inclusions in garnets occur as glassy and polycrystalline

23   inclusions (i.e. nanogranitoids), the latter often organized in mm-sized clusters associated with

24   primary fluid inclusions. Nanogranitoids are characterized by an elliptical faceted shape, with

25   variable sizes ranging from 2 to 115 µm, while glassy inclusions show negative crystal shapes

26   that usually never exceed 15 µm in diameter and present CO_2-rich shrinkage bubbles. The

27   characteristic mineral assemblage observed in nanogranitoids consists of quartz, biotite,

28   muscovite, plagioclase, K-feldspar, kokchetavite and very rarely aluminosilicates. Glassy and

29   re-homogenized melt inclusions are peraluminous and rhyolitic in composition, with $SiO_2 = 69$

30   – 80 wt% and $Na_2O + K_2O = 5 – 12$ wt%. Commonly, the analysed melt inclusions have very

31   high K_2O (> 6 wt%) and very low Na_2O (<2 wt%) contents, indicative for potassic to

32   ultrapotassic melts. Measured H_2O contents of the melts range from 2.9 to 8.8 wt%, whereas

33   CO_2 concentrations are between 160 and 1738 ppm. Accordingly, calculated viscosities for re-

34   homogenized melt inclusions vary between 10^4 and 10^5 Pa·s. Related primary fluid inclusions

35   mainly contain CO_2, with rare occurrence of CO and N_2, and are often associated with quartz,

36   as well as different carbonates and phyllosilicates. It is assumed that the source for the carbonic

37   fluid was external and probably related to the degassing lithospheric mantle. Consequently, it

38   is argued that anatexis was initially triggered by incongruent dehydration melting reactions

39   involving biotite breakdown and proceeded in the presence of an externally derived COH-

40   bearing fluid. The coexistence of COH-bearing fluid and melt inclusions indicates that partial

41   melting occurred under conditions of fluid-melt immiscibility. Potassic to ultrapotassic melt

42   inclusions in UHT granulites suggests that lower crustal anatexis may play a stronger role in

43   the redistribution of heat-producing elements (such as K_2O), potentially influencing the thermal

44   structure of the continental crust.

45

46

47

1. INTRODUCTION

Buoyant andesitic continental crust (e.g. Rudnick, 1995; Taylor & McLennan, 1985) is a distinctive feature that differentiates the Earth from all the terrestrial planets of the Solar System. Although the upper levels of continents can be easily studied and sampled, the structure and chemical composition of the lower continental crust remain mostly enigmatic, due to its inaccessibility for direct observations. Rock xenoliths entrained in lavas and tectonically exposed metamorphic terranes, characterized by mineral assemblages that record lower crustal pressures (i.e. 5-15 kbar), are the only opportunities to obtain useful petrological information on the deep crust. A large number of such exposed terrains has provided a strong evidence that, on a regional scale, the lower continental crust can attain extreme thermal regimes (> 775 °C/GPa; e.g. Harley, 2008; Kelsey and Hand 2015; Brown and Johnson, 2018). Under these conditions, rocks are subjected to ultra-high temperature (UHT) metamorphism, in which peak temperatures exceed 900 °C at typical pressures of 7-13 kbar (Harley, 1998), with important implications for the geochemical differentiation, reworking and rheology of the lower crust (Brown, Korhonen, & Siddoway, 2011; Jamieson, Unsworth, Harris, Rosenberg, & Schulmann, 2011). UHT metamorphism is typically preserved in Mg-Al-rich metapelitic granulites (Brandt, Will, & Klemd, 2007; Harley, Hensen, & Sheraton, 1990; Harley, 2008; Kelsey, 2008; Santosh, Tsunogae, Li, & Liu, 2007), whose diagnostic paragenesis is characterized by the presence of sapphirine + quartz, Al-rich orthopyroxene + sillimanite and osumilite-bearing mineral assemblages (Harley, 1998; Kelsey, 2008). Progressing towards UHT conditions, the lower crust buffers the increasing temperature undergoing extensive partial melting, with the production of felsic magma that may then segregate from its source, leaving behind a more mafic and less fertile residuum (Clemens & Stevens 2016; Sawyer 1994; Sawyer, Cesare, & Brown, 2011; Vielzeuf & Holloway, 1988; White & Powell, 2002). Although S-type granites and granitic leucosomes are the two most prominent products of

crustal anatexis, they do not provide the pristine chemical composition of the felsic anatectic melt, because they are affected by fractional crystallization, crystal accumulation, chemical contamination and presence of xenocrysts (Carvalho, Sawyer, & Janasi 2016; Marchildon & Brown 2001; Milord, Sawyer, & Brown, 2001; Sawyer, 2008; Sawyer et al., 2011; Stevens, Villaros, & Moyen, 2007). Consequently, initial anatectic melt compositions have been mainly deduced from experimental studies (e.g. Clemens, Holloway, & White, 1986; Le Breton & Thompson, 1988; Montel & Vielzeuf, 1997; Stevens, Clemens, & Droop, 1997) and thermodynamic calculations (Grant, 2009; Holland & Powell, 2001; White, Stevens, & Johnson, 2011). Another compelling method to determine the composition of crustal melts during the early stages of anatexis is represented by primary melt inclusions entrapped in peritectic minerals during incongruent melting of metapelitic rocks (Acosta-Vigil, Cesare, London, & Morgan, 2007; Acosta-Vigil et al., 2016; Bartoli et al., 2013; Bartoli, Acosta-Vigil, Tajčmanová, Cesare, & Bodnar, 2016; Cesare, Marchesi, Hermann, & Gómez-Pugnaire, 2003; Cesare, Ferrero, Salvioli-Mariani, Pedron, & Cavallo, 2009; Ferrero et al., 2012; Ferrero, Wunder, Walczak, O'Brien, & Ziemann, 2015). Primary melt inclusions (MI) in high-grade metamorphic rocks typically show variable degrees of crystallization, ranging from glassy to fully crystallized, the latter also referred as *nanogranitoids* (Cesare, Acosta-Vigil, Bartoli, & Ferrero, 2015). Since MI represent droplets of early crustal melt, they preserve precious information on its primordial composition, before the melt is subjected to any chemical change due to magmatic differentiation.

At present, only very few studies have approached a detailed investigation of primary melt and fluid inclusions at UHT conditions (e.g. Cesare et al., 2009; Ferrero et al. 2012; Tacchetto et al., 2019) and therefore the pristine composition of anatectic melts and fluids in UHT rocks is largely unconstrained. In order to overcome this paucity, we report the occurrence of primary MI in peritectic minerals observed in UHT granulites of the Gruf Complex (Central Alps). The

98   aim of this study is to provide a microstructural framework and geochemical characterization

99   of anatectic melts and fluids and evaluate their role during crustal reworking processes

100   associated to UHT metamorphism.

101

102   **2. GEOLOGICAL SETTING**

103   The Penninic units of the Alpine nappe stack in the Central Alps are characterized by mineral

104   isograds, isotherms and isobars that have a concentric shape, defining the so-called "Lepontine

105   Metamorphic Dome" (Todd & Engi, 1997; Wenk, 1955). The Gruf Complex is a ~12 x 10 km

106   migmatitic body between Switzerland and northern Italy, that is located in the south-eastern

107   part of the Lepontine Dome (see Figure 1). To the west the Gruf Complex is delimited by the

108   Adula Nappe, whereas to the north is surrounded by the ultramafic bodies of the Chiavenna

109   Unit and by the crystalline rocks of the Tambo Nappe. To its eastern and southern margin, the

110   Gruf Complex is intruded by the Bergell pluton, a tonalitic to granodioritic calc-alkaline

111   intrusive body that formed between 33 and 30 Ma (Gianola et al., 2014; Oberli, Meier, Berger,

112   Rosenberg, & Gieré, 2004; Samperton et al., 2015; von Blanckenburg, 1992). The southern

113   extremity of the Gruf Complex, and part of the Bergell intrusion, are then cut by the 24 Ma old

114   Novate granite (Liati, Gebauer, & Fanning, 2000), a strong peraluminous S-type granitic stock

115   composed by a swarm of dykes that presumably derived from the partial melting of the

116   surrounding gneissic units (von Blanckenburg, Früh-Green, Diethelm, & Stille, 1992). The

117   dominant lithologies of the Gruf Complex are migmatitic orthogneisses, paragneisses and

118   micaschists (Galli et al. 2011), which underwent upper amphibolite facies migmatisation

119   (Bucher-Nurminen & Droop 1983; Nagel, De Capitani, & Frey, 2002) between 34 and 29 Ma

120   (Galli et al. 2012). These rocks are also associated with irregular tabular bodies of charnockites

121   and leucogranites (Galli et al. 2011). Both migmatitic orthogneisses and charnockites are

122   characterized by the presence of rare sapphirine-bearing granulites, which mainly can be

123   observed as residual enclaves and schlieren (Galli et al. 2011). According to Galli et al. (2011),

124   granulites and charnockites formed at ultra-high temperature conditions of T = 920-940 °C and

125   P = 8.5-9.5 kbar, while migmatisation of the surrounding gneissic and metapelitic lithologies

126   took place at ~740 °C and 6.5-7.5 kbar (Galli, Le Bayon, Schmidt, Burg, & Reusser, 2013).

127

3. ANALYTICAL TECHNIQUES AND EXPERIMENTAL METHODS

129

130   Back-scattered electron (BSE) images and semi-quantitative energy dispersive spectroscopy

131   (EDS) analyses of MI were carried out with a CamScan MX2500 Scanning Electron

132   Microscope (SEM), at the Department of Geosciences of the University of Padova (Italy).

133   Micro-Raman spectroscopy of MI was conducted with a HORIBA Jobin-Yvon LabRAM HR

134   800, equipped with a Nd:YAG laser (λ = 532 nm, laser power on sample ~2-3 mW), at the

135   Institute of Earth and Environmental Science, University of Potsdam. Raman spectra were

136   acquired between 100 and 4000 cm^{-1} with an acquisition time of 20 s during three spectral

137   accumulations. The typical setup also included a grating of 300 lines/mm, a slit width of 100

138   µm and a confocal hole set at 200. Spectral resolution is considered to be of ~10 cm^{-1}, compared

139   to available literature and databases.

140   The chemical composition of garnets was measured with a CAMECA SX50 microprobe,

141   equipped with 4 wavelength dispersive spectrometers, at the C.N.R.-I.G.G. (Consiglio

142   Nazionale delle Ricerche – Istituto di Geoscienze e Georisorse), Department of Geosciences,

143   University of Padova. Analyses were carried out using a focussed beam with a current of 20

144   nA and an accelerating voltage of 15 kV. Counting times for each element were 10 s on peak

145   and 5 s for the background.

146   Major element composition of glass and minerals in the re-homogenized and glassy MI were

147   determined with a JEOL JXA 8200 microprobe at the Department of Earth Sciences

148   (University of Milano, Italy) employing an acceleration voltage of 15 kV, a beam current of 5

149   nA and beam diameter of 1 µm. Acquisition times were 10 s on peak and 5 s for background,

150   measuring Na and K first to avoid diffusional losses. Alkali concentrations were corrected

151   using conservative factors obtained by the analysis of hydrous and anhydrous leucogranitic

152   glasses of known composition. In particular, the standards employed in this study were a 10.1

153   wt% H_2O-bearing glass (LGB 2; Behrens & Jantos, 2001), a 5.5 wt% H_2O-bearing glass (DL;

154   Acosta-Vigil, London, Morgan, & Dewers, 2003) and a nearly anhydrous ($H_2O = 300 \pm 42$

155   ppm) glass (B; Morgan & London, 2005).

156   Single garnet core and rim fragments (~1.5 x 2 mm in size), used for the re-homogenization

157   experiments of the nanogranitoids, were manually separated by cutting from 1.5 mm-thick

158   double-polished thick sections. Two sets of experiments were performed. In the first set, garnet

159   chips were charged into Au capsules (external diameter = 3 mm) alternating them with

160   powdered graphite (granulometry <45 µm). In the second type of experiments, the same gold

161   capsules were filled with alternating layers of garnet chips and powdered SiO_2, obtained from

162   tetraethylorthosilicate (TEOS). In both cases, capsules were crimped and sealed with an arc-

163   welder. Experiments with garnet + graphite charges were conducted using single-stage and

164   end-loaded piston cylinders at the Laboratory for Experimental Petrology, Department of Earth

165   Sciences, University of Milano. Capsules were placed vertically into MgO spacers and then

166   inserted in a NaCl sleeve-pyrex-graphite piston cylinder assembly. The temperature was

167   measured with a K-type (nickel-chromium / nickel-alumel) thermocouple, with an estimated

168   accuracy of ±5 °C and no corrections for the pressure effects on the electromotive force were

169   applied. Experiments were performed at 10 - 12 kbar (i.e. higher then the calculated peak

170   conditions, in order to prevent decrepitation of the inclusions) between 950 °C and 800 °C and

171   with variable run durations (1 to 10 hours). This allowed us to constrain the interval in which

172   re-homogenization was best attained. All runs were first pressurized to 10 - 12 kbar at room

173 temperature and then the assembly was isobarically heated at a constant heating rate (100

174 °C/min) until the targeted temperature was achieved. The experiments were terminated by

175 switching off the power supply, resulting in quenching rates of ~40 °C/s. Capsules were then

176 dissolved in aqua regia and the recovered garnets were singularly mounted in epoxy.

177 Experiments with garnets + quartz charges were performed at the Institute of Geochemistry

178 and Petrology, ETH Zurich, using single stage and end-loaded piston cylinders. The assembly

179 consisted in a talc sleeve, pyrex (only for end-loaded piston cylinder), a graphite furnace and

180 MgO spacers, in which the Au capsules were positioned. Temperature was measured with a B-

181 type ($Pt_{94}Rh_6$ – $Pt_{70}Rh_{30}$) thermocouple. Experiments were performed at 12 kbar, 875 °C and

182 with a duration of 10 h. The experimental procedure was the same used for the experiments

183 with garnets + graphite charges. Although the two set of experiments have slightly different

184 assemblies, it is assumed that this has no relevant influence on the re-homogenization of the

185 inclusions.

186 H_2O and CO_2 contents of remelted inclusions were determined by Nano Secondary Ion Mass

187 Spectrometry (NanoSIMS) employing a Cameca NanoSIMS 50 at Muséum National d'Histoire

188 Naturelle of Paris, following the approaches of Bartoli, Cesare, Remusat, Acosta-Vigil, and

189 Poli (2014) and Créon, Levresse, Remusat, Bureau, and Carrasco-Núñez (2018). Polished

190 experimental capsules with quartz-garnet charges and standard glasses were mounted in

191 indium, to lower the hydrogen background in the analysis chamber (Aubaud et al., 2007), and

192 coated with gold (20 nm thick). Before each analysis, a 5 x 5 µm surface area was initially pre-

193 sputtered for 150 s with a 170 pA primary Cs^+ rastering beam, in order to remove the gold

194 coating and reach a sputtering steady-state (Thomen, Robert, & Remusat, 2014). Subsequently,

195 the primary Cs^+ beam was set at 17 pA and scanned over a surface area of 3 x 3 µm.

196 Nevertheless, to avoid surface contamination, only ions from the inner 1 x 1 µm region were

197 collected with the "beam blanking mode". Exposed MI were analysed through collection of

198   secondary ions of $^{12}C^-$, $^{16}OH^-$, $^{28}Si^-$ and $^{56}Fe^{16}O^-$ in multicollection mode. Mass resolving power

199   was set at minimum 5500, enough to resolve interferences on $^{16}OH^-$. Each analysis consisted

200   in a stack of 200 cycles, with a duration of 1.024 s for every single cycle. The vacuum in the

201   analysis chamber never exceeded 2.5 x 10^{-10} Torr during the entire session of measurements.

202   H_2O and CO_2 contents of the glasses were quantified measuring $^{16}OH^-/^{28}Si^-$ and $^{12}C^-/^{28}Si^-$ ratios,

203   respectively (Bartoli et al., 2014, Créon et al., 2018). These ratios were converted into

204   concentrations using calibration curves obtained from standards of known composition.

205   Standards for the determination of H_2O included two standards used for the alkali correction

206   (DL and B, see above) plus an additional hydrous glass with 4.3 wt% H_2O (LGB1; Behrens &

207   Jantos, 2001). On the other hand, standards for CO_2 consisted in four trachyandesites (STR 9,

208   10, 11 and 13) from the Stromboli volcano, experimentally doped in carbon and water by

209   Bureau et al. (2003). Concentrations and uncertainties were calculated using the R program,

210   following the procedure described in Bartoli et al. (2014) and Thomen, Robert, & Remusat

211   (2014). Average major element and volatile concentrations of the analysed MI are reported in

212   Table 1.

213

214   **4. RESULTS**

215

216   **4.1 Mineral assemblages of the UHT granulites**

217   All the investigated samples were collected in the lower part of Val Codera, near the locality

218   of Bresciadega (see also Galli et al., 2011). Two varieties of UHT granulite with granofelsic

219   texture were studied (Figure 2). The first type corresponds to type A of Galli et al. (2011) and

220   consists in a dark, massive granulite containing large garnet (up to 2 cm) and sapphirine (up to

221   5 mm) porphyroblasts, associated with a matrix of up to 3 mm-sized orthopyroxene (Opx),

222   cordierite (Crd), biotite (Bt) and K-feldspar (Kfs). Garnet (Grt) appears as faint pink, rounded

223   crystals showing a clear zonation. Numerous mineral inclusions of biotite, orthopyroxene,

224   sapphirine, plagioclase (Pl), cordierite, rutile (Rt), ilmenite, sillimanite, tourmaline, apatite

225   (Ap), spinel, staurolite, corundum, monazite and zircon can be observed within the

226   porphyroblastic garnets. On the other hand, sapphirine (Spr) is generally hypidiomorphic,

227   prismatic and pleochroic (from pale-red to blue), showing sometimes a longitudinal, simple

228   twinning system.

229   The second type of granulite belongs to type C of Galli et al. (2011). The rock is massive and

230   melanocratic with a mineral assemblage made of porphyroblastic garnet (up to 1.5 cm),

231   porphyroblastic orthopyroxene (<1.5 mm), biotite, cordierite, sillimanite and symplectitic

232   spinel. Sapphirine may be present as symplectitic grains in the rock matrix, or as small (<500

233   µm) inclusions within garnet. Other mineral inclusions observed within garnet grains are:

234   biotite, quartz, sillimanite, cordierite, plagioclase, spinel, zircon, apatite, corundum, rutile,

235   staurolite and tourmaline.

236   In both granulites, melt inclusions (MI) are mainly present in the porphyroblastic garnets,

237   where they may occur as single, scattered inclusions or may form mm-large clusters. These

238   clusters are commonly found in the cores of the garnets (Figure 3a-b), but their occurrence

239   towards to the rims has been also noticed (Figure 3c-d). The presence of different birefringent

240   crystals under crossed polars (Figure 3e-f) indicates that the majority of MI are polycrystalline

241   (i.e. nanogranitoids; Cesare et al. 2015). Often, fluid inclusions, usually showing a distinctive

242   darker appearance and high birefringence (Figure 3g), occur associated to nanogranitoids

243   within the same clusters. Moreover, sporadic glassy inclusions containing shrinkage bubbles

244   have been also observed (Figure 3h). In contrast to polycrystalline MI, glassy MI occur

245   exclusively as single inclusions dispersed in the garnets, without forming clusters, although

246   occasionally, glassy MI may occur close to nanogranitoids. Moreover, rare MI with multiple

247   birefringent phases have been also identified in sapphirine porphyroblasts of Type A granulites

248 (Figure 3i). The MI in sapphirine are too rare to allow their experimental re-melting, but were

249 characterized by Raman spectroscopy.

250

251 **4.2 Micro-Raman characterization of glassy, nanogranitoid and fluid inclusions**

252 Micro-Raman investigations for the glassy inclusions observed in Type A samples show that

253 the glass is hydrous (see Figure 4a). Furthermore, the single Raman band displayed at 1382

254 cm^{-1} (Figure 4a) indicates that some dissolved molecular CO_2 is also present in the melt

255 (Brooker, Kohn, Holloway, McMillan & Carroll, 1999; Ni & Keppler 2013). Shrinkage

256 bubbles in the glass contain CO_2, as demonstrated by the presence of the "Fermi-doublet" in

257 the Raman spectra (see Figure 4a). Densities of CO_2 in these bubbles (see Table S1), calculated

258 with the densimeter of Wang et al. (2011), range between 0.5 and 0.8 g/cm^3 ($\pm$ 0.3 g/cm^3).

259 Raman analyses showed that nanogranitoids (Figure 4b,c) may contain quartz, muscovite,

260 phlogopite, K-feldspar, kokchetavite (a polymorph of $KAlSi_3O_8$) and an unknown phase with

261 a main Raman peak at 430 cm^{-1}. Unexpectedly, Raman investigations also showed that some

262 of these nanogranitoids could retain some CO_2 bubbles (Figure 4b,c), suggesting the existence

263 of micropores. Nanogranitoids observed in sapphirine crystals from type A granulites (Figure

264 4d) contain quartz, muscovite, kokchetavite and the unknown phase with the peak at 430 cm^{-1}.

265 Fluid inclusions (FI), present in both granulites, display a fluid fraction as well as a solid

266 portion, in which several phases were identified. In type A granulites (together with CO_2)

267 muscovite, Fe-magnesite, calcite, pyrophyllite, quartz and biotite were the most common

268 phases. On the other hand, type C granulites have FI composed of – in addition to the same

269 phases observed for type A – paragonite, magnesite, siderite, phlogopite, N_2 and CO (Figure

270 4e,f). For one inclusion it was possible to calculate the relative amount of components in the

271 fluid, applying the method of Dubessy, Poty, and Ramboz (1989). The obtained molar fractions

272 were 94 mol% for CO_2 and 6 mol% for N_2. For what concerns the carbonate phases, Fe-

273　magnesite in FI of both granulites has variable Fe content (Fe# = 100 x Fe/(Fe + Mg + Mn +

274　Ca + Al), as defined by Boulard, Guyot, & Fiquet, 2012), typically ranging between Fe# = 20

275　and Fe# = 55. Calculated CO_2 densities (Wang et al. 2011) for FI in type A granulites vary

276　between 0.3 and 1.0 g/cm^3 (see Table S1), a range comparable to that calculated for type C

277　granulites (0.4-0.8 g/cm^3). It is also remarkable to notice that, neither in the shrinkage bubbles

278　of glassy inclusions nor in fluid inclusions, H_2O was detected.

279

280　**4.3 Microstructures of nanogranitoids**

281　Detailed observations with SEM allowed to determine the principal microstructural features of

282　nanogranitoids, as well as their mineral assemblage. Typically, MI of both Type A and C

283　granulites have an elliptical faceted shape, with major axes ranging between 2 and 115 µm

284　(Figure 5a-f). Nevertheless, for Type A, the size of MI decreases from rims to cores. MI in the

285　rims have an average size of 47 ± 5 µm, those found in the intermediate region of the garnets

286　(i.e. between cores and rims) are 35 ± 5 µm, while MI found in the cores have an average size

287　of 24 ± 3 µm. Together with nanogranitoids with a nearly negative crystal shape (Figure 5a,b),

288　some MI display natural decrepitation, with offshoots that are arranged radially around the

289　inclusions (Figure 5c,d). The number of offshoots per inclusion varies drastically (from 1 to

290　10), with larger inclusions showing more (and usually longer) offshoots. The calculated

291　average length of the offshoots for MI <45 µm in size is 6 µm, whereas MI bigger than 45 µm

292　have an average length of the offshoots of 13 µm. Glassy inclusions in Type A granulites show

293　negative crystal shapes and their size is <15 µm (average diameter: 8 µm). MI in type C

294　granulites also have an elliptical faceted shape and show a polycrystalline nature. However, in

295　contrast to MI in type A granulites, they have similar sizes from core to rim and hardly exceed

296　40 µm in diameter, with an average length of the major axis of 21 ± 2 µm. Also garnets from

297 type C granulites show some decrepitated MI (Figure 5e,f), which have an average length of

298 the offshoots of 5 μm.

299 In general, the mineral assemblage within nanogranitoids has an inequigranular and interlobate

300 fabric composed of mainly hypidiomorphic crystals of quartz, biotite, muscovite, plagioclase,

301 K-feldspar and very rarely aluminosilicates (Figure 5a-f). Sometimes nanogranitoids clearly

302 display an igneous microstructure defined by intergrowths of quartz, feldspars and biotite. SEM

303 analyses also highlighted the presence of accessory minerals, typically Cl-bearing apatite and

304 rutile, which are usually more idiomorphic compared to the other phases (Figure 5d,e).

305

306 **4.4 Chemical composition of host garnets and minerals in nanogranitoids**

307 In this section we report only chemical analyses of garnet porphyroblasts. For detailed chemical

308 analyses of all rock-forming minerals see Galli et al. (2011). Analysed garnets of Type A and

309 Type C granulites are almost pure almandine-pyrope solid solutions and display a zonation

310 marked by pyrope-richer rims (Type A = $Alm_{43-50}Prp_{44-53}Sps_{0-2}Grs_{2-6}$; Type C = $Alm_{44-54}Prp_{43-}$

311 $_{55}Sps_{0-1}Grs_{1-3}$) compared to cores (Type A = $Alm_{47-52}Prp_{39-48}Sps_{1-3}Grs_{3-9}$; Type C = Alm_{50-}

312 $_{62}Prp_{32-47}Sps_{0-1}Grs_{2-6}$).

313 For what concerns the nanogranitoids, their size often hampers a precise chemical

314 characterization of their mineral assemblage. Nevertheless, some nanogranitoid inclusions in

315 Type A granulites were large enough to allow the chemical analysis of the single mineral

316 phases (see Table S2). Plagioclases show variable X_{An} [An / (An + Ab)] between 0.10 (albite)

317 and 0.49 (andesine). By contrast, biotites are Ti-free and characterized by X_{Mg} [Mg / (Mg +

318 Fe^{2+})] ranging from 0.71 to 0.86. Other K-rich phases that have been recognized are K-feldspar

319 and phengite (Ph), the latter displaying a $X_{Mg} = 0.59$.

320

321

4.5 Remelted nanogranitoids

Experiments between 900 and 875 °C produced the most homogenized glasses. Remelted MI are typically <15 µm in size and display elongated to perfect negative crystal shapes (Figure 6a-d). Some inclusions, together with glass, display mineral phases like rutile and apatite that indent the walls of the MI (Figure 6c). These phases are interpreted to be accidental minerals trapped during the formation of the inclusions, since they are observed before and after the re-homogenization experiments. Therefore, they are not daughter minerals (i.e. phases that crystallized directly from the melt; e.g. Ferrero et al., 2012; Acosta-Vigil et al. 2016). Moreover, few MI may also exhibit bubbles (Figure 6d), suggesting that the fluid underwent incomplete dissolution in the melt during the experimental run or alternatively it diffused during cooling to form shrinkage bubbles (Lowenstern, 1995). A little fraction of the analysed MI population is characterized by the presence of unmelted daughter minerals, testifying incomplete remelting (Figure 6e,f). Typical daughter minerals coexisting with glass are euhedral to subhedral biotite grains ($X_{Mg} = 0.82 – 0.88$ and $TiO_2 < 0.2$ wt%, see Table S3) and rounded quartz crystals.

Experiments with garnets + quartz charges at 875 °C produced substantial amounts of melt in the matrix outside the garnets (Figure 6g), that infiltrated within the garnet crystals and led to the formation of large pockets of melt. These melt pockets differ microstructurally from remelted MI by their size (commonly >20 µm in diameter, although few of them have sizes comparable to remelted MI) and by the striking abundance of bubbles, a feature that indicates high fluid contents (Figure 6h). The matrix melt derives from the melting of mineral intergrowths or matrix phases, such as biotite and feldspar, which could not be avoided during the manual crushing of the garnet chips. Often, a peritectic reaction between the melt and the garnet can be observed, with the formation of orthopyroxene or corundum (Figure 6g).

346   Evidence of overheating in the MI has been observed at all temperatures, but predominantly at

347   950 °C. This is indicated by the formation of peritectic phases such as orthopyroxene or gedrite

348   (Figure 6i), by the recrystallization of new garnet within the inclusion or by a change in the

349   chemical composition of the garnet around the remelted inclusions. Chemical analyses (see

350   Table S3) for peritectic orthopyroxenes indicate that they are Al-rich (8.3 – 10.4 wt% at 950

351   °C and 6.5 – 9.2 wt% Al_2O_3 at lower temperature), with $X_{Mg} = 0.69$ - 0.73 (at 950 °C) and 0.67

352   – 0.84 (at 900-875 °C). These compositions are comparable to those measured in the

353   orthopyroxene porphyroblasts in the matrix of granulites (Galli et al. 2011). One analysis of a

354   recrystallized garnet 950 °C shows that the new garnet is Fe-poorer and Mg-richer ($X_{Mg} = 0.64$)

355   compared to the original garnet composition ($X_{Mg} = 0.47$). Since at 950 °C microstructural

356   evidence for overheating is dominant, the glasses analysed at these conditions were considered

357   not representative and therefore disregarded (Figure S1). For what concerns the experiments

358   performed at 800 °C, MI often display incomplete remelting and only rare homogeneous

359   glasses could be found. This might indicate that this temperature corresponds to the lower

360   boundary for remelting experiments.

361

362   **4.6 Chemical composition of glasses**

363   Figure 7a-b and Table S4 report chemical analyses of glasses for remelted inclusions and for

364   preserved glassy inclusions, all recalculated on anhydrous basis. For what concerns

365   experimentally   remelted   MI,   analyses   that   displayed   clear   evidence   for

366   contamination/interaction with the host garnet, or mixing with matrix melt, were discarded and

367   were not discussed (see Figure S1). Glasses are dominantly peraluminous (ASI = 1.0 – 1.6,

368   $[Al_2O_3/(CaO+Na_2O+K_2O)]_{molar}$), with only two MI that fall into the peralkaline field. Natural

369   glassy inclusions have a slightly more restricted range (ASI = 1.0 – 1.1) compared to re-

370   homogenized nanogranitoids. With rare exceptions, analysed MI are corundum-normative (Crn

= 0.2 – 4.88, see Table S4). Both re-homogenized MI and glassy inclusions are predominantly rhyolitic in composition, with SiO_2 = 68.6 - 79.7 wt% and Na_2O+K_2O = 5.3 - 12.0 wt% (on anhydrous basis), developing a negative correlated trend in the SiO_2 vs. Na_2O+K_2O space (Figure 7b). However, melts with a trachytic composition have been also observed, as shown by one MI from Type A granulite remelted at 875 °C. Glassy inclusions have slightly higher total alkali contents compared to remelted nanogranitoids. Plotted in Harker variation diagrams (Figure 8 a-f), glassy and re-homogenized inclusions show a clear increase in Al_2O_3 and K_2O with decreasing SiO_2. By contrast, CaO, $FeO+MgO+TiO_2$, Na_2O and Cl display more scattered distributions. Glassy inclusions differ from re-homogenized nanogranitoids by their low CaO (<0.2 wt% vs. 0.2-2.0 wt%) and $FeO+MgO+TiO_2$ (<1.4 wt% vs. 1.4-3.4 wt%) concentrations. All the analysed melt inclusions are characterized by a decoupling in the alkali content, with most inclusions showing Na_2O concentrations <2 wt% and K_2O > 6 wt%. Re-homogenized MI have variable K# ratios [K# = molar $K_2O/(K_2O+Na_2O)$ x100], ranging from 72 to 98 (average: 87 $\pm$ 4) for Type C granulites and from 56 to 82 (average: 71 $\pm$ 8) for Type A granulites. Similarly, glassy inclusions from Type A granulites have K# between 59 and 87 (average: 77 $\pm$ 5).

H_2O and CO_2 concentrations of remelted inclusions, determined by NanoSIMS, are reported in Table 2 and shown in Figure 9. H_2O contents in the analysed MI range from 2.9 to 8.8 wt%, without any clear distinction between garnet cores and rims. Indeed, calculated averages are 6.2 $\pm$ 1.3 wt% (type A) and 7.1 $\pm$ 3.0 wt% (type C) for garnet cores, whereas for garnet rims is 4.4 $\pm$ 0.9 (type C). By contrast, CO_2 concentrations allow to subdivide the analysed MI into two distinct families, one clustering at ~1200 ppm and the other showing concentrations <500 ppm. From Figure 9 it is also possible to notice that MI with low CO_2 concentrations are characterized by a narrower range in H_2O (4.1 – 5.5 wt%) compared to MI with higher CO_2 contents.

5 DISCUSSION

5.1 Anatexis at UHT conditions

The mineral assemblage displayed by nanogranitoid inclusions within the peritectic garnet of the studied granulites indicates that these inclusions represent droplets of pristine felsic melt, an observation that was also confirmed by the measurement of their chemical composition after remelting experiments. Therefore, the investigated MI allow firstly an appraisal of the melting regime on the regional scale and secondly, a better constraint on crustal anatexis under UHT conditions.

Granulites from the Gruf Complex are characterized by the presence of glassy and nanogranitoid inclusions. Their coexistence at the micrometric scale indicates that the melt behaves differently when it is trapped within pores. Glassy inclusions are on average smaller than nanogranitoids and therefore their preservation may be explained by inhibition of crystallization (Cesare et al., 2009) due to the greater supersaturation required by smaller pores to develop crystals compared to larger ones (Holness & Sawyer, 2008). Alternatively, lower H_2O contents and, in turn, higher viscosities in some inclusions could have inhibited the nucleation with the formation of glass (Bartoli, Acosta-Vigil, & Cesare, 2015). A different volatile content in glassy and crystallized melt inclusions seems to be supported by the different electron microprobe totals (Table 1). The chemical composition of re-homogenized MI is consistent with the mineral assemblage observed in the nanogranitoids. This can be also observed in the AKF diagram (Figure 10), where analysed glasses for Type A granulites plot within the triangle defined by the tie-lines of the minerals measured in the non-remelted nanogranitoids. Although the chemical composition of the minerals forming MI in Type C granulites could not be measured (Figure 10b), it is assumed that the mineral assemblage should be similar to the one noticed for Type A granulites and therefore an equivalent triangle for MI in Type C granulites is expected. From Figure 10a it is also possible to observe that glassy

421 inclusions plot towards the K-apex of the triangle, while remelted MI tend to be more scattered,

422 with some analyses plotting slightly outside the triangle defined by the mineral assemblage. In

423 the Qz-Ab-Or normative diagram (see Figure S2) glassy and re-homogenized inclusions from

424 the Gruf Complex plot close to the Qz-Or join, considerably away from the haplogranite ternary

425 eutectic. Furthermore, MI also plot at lower Ab-contents compared to charnockites,

426 leucogranites and S- and A-type granites, but overlap the field displayed by MI from the Kerala

427 Khondalite Belt, consistent with their UHT nature.

428 Figure 8 shows that the analysed glasses have markedly different compositions compared to

429 the charnockites of the Gruf Complex, indicating that the charnockites might have been

430 generated from another metapelitic source or during a melting event unrelated with the

431 formation of the granulites. By contrast, MI have similar concentrations for CaO, Al_2O_3 and

432 $FeO+MgO+TiO_2$ compared to the leucogranites that intrude the migmatitic paragneisses and

433 micaschists (see Galli, Le Bayon, Schmidt, Burg, & Reusser, 2013). Moreover, MI overlap the

434 trend displayed by the melt inclusions from the Kerala Khondalite Belt (Cesare et al. 2009;

435 Ferrero et al. 2012), even though the latter have slightly higher $FeO+MgO+TiO_2$ and Cl

436 concentrations. On the other hand, MI from the Gruf Complex have different trends for

437 $FeO+MgO+TiO_2$, alkalis, and partly CaO, compared to A- and S-type granites. This evidence

438 strongly reinforces the assumption that S- and A-type granites do not mirror primary crustal

439 melts, but liquids modified by a large plethora of mechanisms during their production and

440 segregation from the source (see Introduction).

441 MI are characterized by high K_2O and low Na_2O concentrations compared to regional

442 charnockites and leucogranites, but also relative to A-and S-type granites (Figure 8d-e).

443 However, a decoupled behaviour in alkali contents has been also noticed in the MI from the

444 Kerala Khondalite Belt (KKB, S-India), in which ultrapotassic rhyolitic melts have been

445 reported (Cesare et al. 2009; Ferrero et al., 2012). It is generally believed that khondalites from

the KKB originated during crustal anatexis at UHT conditions (Nandakumar and Harley, 2000; Yu, Santosh, Li, & Shaji, 2019) and therefore it seems that high K_2O/Na_2O ratios are a distinctive feature of anatectic melts at extremely high crustal temperatures. K-rich melts have also been experimentally derived by Patiño Douce and Johnston (1991) from a pelitic starting material. In particular, their experiments between P = 7-13 kbar and T = 875-1075 °C give K_2O-rich and Na_2O-poor liquids that closely resemble MI from the Gruf Complex and the KKB. Additionally, Droop, Clemens, & Dalrymple (2003) obtained K-rich melts (K_2O/Na_2O = 4.1 - 9.5) from partial melting experiments of metapelitic micaschists at 900 °C and 5 kbar. In the AKF diagram (Figure 10) analyses for the KKB, as well as the experimental glasses of Droop et al. (2003) and Patiño-Douce & Johnston (1991), plot towards the K-apex, overlapping in part the field formed by the MI of the Gruf Complex. The fact that K-rich melts are observed up to UHT conditions, independently of the pressure, may be explained by the role of titanium in expanding the stability field of biotite towards higher temperatures. Consequently, the melting of biotite may be delayed, compared to the melting of sodic plagioclase, leading to an enrichment of potassium in the melt.

All this evidence suggests that melts produced at the onset of anatexis under high to ultra-high temperature conditions are dominantly potassic to ultrapotassic, as was also recognized in previous studies (Cesare et al., 2009; Ferrero et al., 2012).

5.2 Volatiles in the deep crust

Primary clusters of melt and fluid inclusions occur typically in both garnet cores and rims of the granulites from the Gruf Complex, indicating that they were entrapped during the same anatectic event. The coexistence of CO_2 with stepdaughter phases such as carbonates (Fe-magnesite, siderite and calcite) and phyllosilicates (pyrophyllite, muscovite and biotite) within FI strongly suggests that the original fluid had a COH(N) composition. Nevertheless, the

471 presence of K-rich phases such as muscovite and biotite might also indicate that some of the

472 FI are instead mixed inclusions (fluid + melt) and therefore part of the H_2O may derive from

473 the melt. Similar mixed inclusions were documented in garnet of crustal enclaves (Cesare,

474 Maineri, Baron Toaldo, Pedron, & Acosta-Vigil, 2007) and anatectic granitoids (Ferrero,

475 Braga, Berkesi, Cesare, & Laridhi Ouazaa, 2014). Although H_2O as a free phase has been never

476 demonstrated by Raman spectroscopy within the measured FI of the Gruf Complex, its

477 occurrence on the nanometric scale cannot be excluded (see also Lamadrid, Lamb, Santosh, &

478 Bodnar, 2014; Esposito et al., 2016). On the other hand, carbonates and phyllosilicates are

479 interpreted as re-speciation products after post-entrapment carbonation and hydration reactions

480 between garnet host and fluid, as it has been suggested also for other HT/UHT terranes (Ferrero

481 et al. 2014; Tacchetto et al., 2019; Carvalho et al., 2019). Hence, the different densities

482 displayed by the FI are a direct consequence of incomplete reactions, which leave a variable

483 amount of CO_2 in the residual fluid.

484 Raman spectroscopy measurements allowed to confirm the presence of CO_2 and H_2O in glassy

485 and nanogranitoid inclusions (see Fig. 4), indicating that both inclusions derived from the

486 similar melt. The ubiquity of pure CO_2-rich shrinkage bubbles (without any apparent detectable

487 H_2O, see discussion above) within glassy inclusions can be explained by the preferential

488 partition of H_2O into silicate melt than CO_2 (e.g. Holtz, Johannes, Tamic, & Behrens, 2001;

489 Tamic, Behrens, & Holtz, 2001). Further investigations with NanoSIMS enabled the

490 quantification of the minimum volatile component dissolved in this melt. The dissolved H_2O

491 measured in the MI displays a wide spectrum (2.9-8.8 wt%), with a large proportions of the

492 analyses that have >5 wt%. Such values indicate that crustal melts at T ~ 900 °C can have

493 higher H_2O contents than commonly assumed for the haplogranitic system. However, as

494 pointed out by Holtz et al. (2001), this behaviour is to be expected for melts that markedly

495 differ from eutectic compositions and that involve the breakdown of micas in the melting

496 reaction, conditions which are both realised for the MI from the Gruf Complex. Moreover,

497 analogous H_2O contents have been also observed in MI from the granulites and upper

498 amphibolite-facies migmatites from the Strona Valley, in the Ivrea Zone (Carvalho et al.,

499 2019). It is therefore suggested that, at HT/UHT conditions, anatectic rhyolitic melts have

500 considerable but uneven H_2O contents, which may strongly affect the mobility of these

501 magmas. Variable water contents in anatectic melts were also recognized by Bartoli et al.

502 (2014) in peritectic garnets of amphibolite-facies migmatites close to the Ronda peridotite and

503 were interpreted to represent micro-scale buffered compositions due to heterogeneous domains

504 in the protholith. A similar mechanism might be envisaged also for the MI of the Gruf Complex,

505 since low and high values sometimes can be found in the same garnet crystal. Another striking

506 feature of the analysed MI is the marked difference in the CO_2 contents (Figure 9), with

507 inclusions forming two distinct groups. The highest CO_2 concentrations are nearly identical to

508 those observed in MI from granulites and amphibolites from the Ivrea Zone (see also Carvalho

509 et al., 2019), whereas the "CO_2-depleted" MI plot at lower values.

510 Our results clearly demonstrate that the peritectic garnets of the investigated UHT granulites

511 grew with coexisting COH-bearing fluids and silicate melts, that, due to the low solubility of

512 CO_2 in silicate melts (Holtz et al., 2001; Tamic et al., 2001), led to fluid-melt immiscibility.

513 The origin of the COH fluid in high-grade metamorphic rocks has been often source of debates.

514 The granulites from the Gruf Complex lack graphite in their mineral assemblage and therefore

515 an internal origin for carbon seems to be unlikely. However, the absence of graphite in the

516 rocks does not preclude the possibility that graphite was present in the original mineral

517 assemblage and was completely consumed before or during anatexis. Another source for

518 carbon may be represented by carbonaceous sediments interlayered in metapelitic rocks. In the

519 Gruf Complex very thin carbonate layers have been recognized only at the contact with the

520 ultramafic Chiavenna Unit, but never within the migmatitic gneisses that host the UHT

521 granulites and thus a sedimentary source for carbon does not seem a convincing argument.

522 Accordingly, we infer that CO_2 was externally introduced in the lower crust, very likely from

523 a mantle source. This is in agreement with previous studies that suggested the mantle as a

524 common source for CO_2 in high temperature granulites (e.g. Hoefs & Touret, 1975; Jackson,

525 Mattey, & Harris, 1988; Santosh & Omori, 2008; Touret & Huizenga, 2011). However, we

526 also emphasize that without a rigorous isotopic determination for carbon, the origin of CO_2

527 remains uncertain. On the other hand, the minor N_2 amount detected in Type C granulites is

528 interpreted to derive from the breakdown of NH_4^+-bearing micas during anatexis (e.g. Moin,

529 Guillot, & Gibert, 1994; Cesare et al., 2007).

530 For the Gruf Complex, if an external source for CO_2 is assumed, the different CO_2

531 concentrations in the MI may be related to small-scale heterogeneities of the fluid composition

532 within the matrix surrounding the growing peritectic garnets.

533

534   **5.3 Rheology of anatectic melt**

535 Granulites from the Gruf Complex represent UHT residues of metapelitic lower crustal rocks,

536 attesting that substantial partial melting (~40 - 50%, Galli et al., 2011) occurred in the

537 lowermost portions of the continental crust. This partial melting generated rhyolitic melts that

538 are now preserved in the MI found in the peritectic garnets of the investigated granulites. An

539 important aspect related to the genesis of anatectic rhyolitic melts is to determine some

540 fundamental physical properties that govern the mobilization of these melts through the crust,

541 such as viscosity and density. The complete analysis (geochemistry and water content) of four

542 MI allowed us to calculate the viscosity of the melt. Assuming a temperature of 875 °C, which

543 corresponds to the experimental temperature, and applying the equation of Scaillet, Holtz,

544 Pichavant, & Schmidt (1996), viscosities vary between $10^{3.9}$ and $10^{4.5}$ Pa·s. These values are

545 comparable to those calculated using the equation of Giordano, Russell, & Dingwell (2008),

546 which range between $10^{4.1}$ and $10^{4.8}$ Pa·s and are ~2 orders of magnitude lower than for

547 commonly assumed nearly anhydrous crustal melts at 900 °C. The calculated viscosities for

548 the melt during incipient UHT anatexis are consistent (within error) with the experimental

549 values obtained by Ardia, Giordano, and Schmidt (2008) for rhyolitic melts between 5 and 15

550 kbar at similar water contents (see Figure S3). Moreover, viscosities for MI from the Gruf

551 Complex overlap the range of viscosities obtained by Bartoli et al. (2013) for metatexites within

552 the metasedimentary sequence at the contact with the Ronda peridotite, in the Spanish Betic

553 Cordillera.

554 Combining viscosities with the respective densities allowed us to speculate on the ascent

555 velocity of the melt from its source. Our calculations were based on a simple porous flow model

556 (Turcotte & Schubert, 2002) and assuming an average density of 3.1 g/cm^3 for the lower crust

557 (Hacker, Kelemen, & Behn, 2015), a porosity of 8% (which corresponds to the liquid

558 percolation threshold of Vigneresse, Barbey, & Cuney, 1996) and a grain size for the matrix of

559 1-2 mm. For an average melt viscosity of $10^{4.4 \pm 0.3}$ Pa·s and an average density of 2.3 g/cm^3

560 (determined with the program DensityX by Iacovino and Till, 2019), melt velocities of 5-83

561 mm/year were calculated (see Table S5). Hence, if only porous flow is considered, at least tens

562 of thousands of years are needed before the melt will move at distances >1 km. At high melt

563 fractions it is expected that the pervasively distributed melt might be channelized by porosity

564 waves (e.g. Connolly & Podladchikov, 2015), resulting in an enhanced melt migration rate.

565 Furthermore, it has to be stressed that the calculated velocities are relative to a static solid

566 matrix. However, melting in the lower crust occurs in a dynamic environment, in which

567 deviatoric stresses may largely increase the ascent velocity of magmas (Sawyer 1994).

568 The Gruf Complex is as an example of upward extruded lower continental crust (Galli et al.

569 2012; Galli et al. 2013), that most probably was exhumed as a crustal diapir and for which an

570 exhumation rate of ~2 mm/year was estimated (Droop and Bucher-Nurminen, 1984). This

571 velocity is lower compared to those calculated for the anatectic melt and therefore it might be

572 plausible that the melt (or at least part of it) may have been effectively segregated from the

573 ascending migmatitic body. However, it is also expected that melts with physical properties

574 similar to those of the Gruf Complex may undergo less segregation if they are produced in

575 faster exhumed crustal sections. Field observations and numerical modelling (e.g. Ganguly,

576 Dasgupta, Cheng, & Neogi, 2000; Gerya, Perchuk, & Burg, 2008; Whitney, Teyssier, & Fayon,

577 2004) indicate that hot and partially molten crust may rise with velocities up to 50 mm/year,

578 i.e. in the range of those calculated in this study. Therefore, on the small scale, melts may

579 segregate from the source (forming leucosomes), but on the large scale they would probably

580 move coupled with the ascending hot crust (Teyssier & Whitney, 2002). Consequently,

581 segregation processes in migmatitic crustal domains should be evaluated also taking into

582 account the exhumation rate of the crust, and not only the ascent velocity of the melt. Although

583 the proposed approach might be simplistic, it gives a first-order approximation on the

584 ascending behaviour of pristine anatectic melts at the onset of crustal anatexis under UHT

585 regime.

586

6. CONCLUSIONS

588 Evidence that the Earth's continental crust has the ability to attain, on a regional scale, ultra-

589 high temperatures has been widely reported. Under these conditions, middle and lower crust

590 undergo substantial modifications that have important consequences on their rheological

591 properties, which, in turn, may largely affect the mass transfer at the crust-mantle boundary.

592 Peraluminous, K-rich rhyolitic melt inclusions observed in garnet porphyroblasts of UHT

593 granulites from the Gruf Complex are the result of crustal anatexis, the latter driven by the

594 breakdown of biotite. The presence of primary melt and fluid inclusions with both a COH

595 volatile component suggests that anatexis initially started due to dehydration melting reactions

596 and was promoted by the influx of an external $CO_2 + H_2O$ fluid. Although the source of CO_2

597 cannot be undoubtedly ascertained, we infer that a mantle origin for the carbon is a more likely

598 explanation. On the other hand, the high H_2O content measured in the melt inclusions suggests

599 that anatectic melts at UHT conditions are less dry than commonly assumed, with relevant

600 implications for the viscosity of anatectic melts. The production of low density rhyolitic melts

601 in the lower crust may induce large-scale weakening (Rosenberg and Handy, 2005) that

602 ultimately may lead to the lateral flow of mountain belts (Jamieson et al. 2011) or to the

603 formation of domes and crustal diapirs (e.g. Gerya, Perchuk, Maresch, & Willner, 2004;

604 Teyssier & Whitney, 2002). The latter mechanism can be an effective geological process that

605 may trigger the exhumation of high-grade metamorphic rocks. Moreover, the potassic to

606 ultrapotassic composition of the analysed anatectic melts may indicate that crustal anatexis can

607 have a larger impact in the redistribution of heat-producing elements (such as K_2O), with

608 important implications for the thermal structure of the continental crust.

609 This study shows that anatectic melt inclusions provide a fundamental insight into the

610 comprehension of the melting regime in UHT terranes and the chemical differentiation of the

611 lower crust.

612

613 **ACKNOWLEDGEMENTS**

614

622

References

624

625 Acosta-Vigil, A., London, D., Morgan, G. B., & Dewers, T. A. (2003). Solubility of excess

626 alumina in hydrous granitic melts in equilibrium with peraluminous minerals at 700–

627 800 °C and 200 MPa, and applications of the aluminum saturation index. *Contributions*

628 *to Mineralogy and Petrology*, *146*, 100-119.

629 Acosta-Vigil, A., Cesare, B., London, D., Morgan, G.B. (2007). Microstructures and

630 composition of melt inclusions in a crustal anatectic environment, represented by

631 metapelitic enclaves within El Hoyazo dacites, SE Spain. *Chemical Geology, 237*,

632 450-465.

633 Acosta-Vigil, A., Barich, A., Bartoli, O., Garrido, C.J., Cesare, B., Remusat, L., Poli, S.,

634 & Raepsaet, C. (2016). The composition of nanogranitoids in migmatites overlying

635 the Ronda peridotites (Betic Cordillera, S Spain): the anatectic history of a

636 polymetamorphic basement. *Contributions to Mineralogy and Petrology, 171,* 1-31.

637 Ardia, P., Giordano, D., & Schmidt, M. W. (2008). A model for the viscosity of rhyolite as a

638 function of H_2O-content and pressure: A calibration based on centrifuge piston cylinder

639 experiments. *Geochimica et Cosmochimica Acta*, *72*, 6103-6123.

640 Aubaud, C., Withers, A. C., Hirschmann, M. M., Guan, Y., Leshin, L. A., Mackwell, S. J., &

641 Bell, D. R. (2007). Intercalibration of FTIR and SIMS for hydrogen measurements in

642 glasses and nominally anhydrous minerals. *American Mineralogist*, *92*, 811–828.

643   Bartoli, O., Cesare, B., Poli, S., Bodnar, R.J., Acosta-Vigil, A., Frezzotti, M.L., & Meli, S.

644   (2013). Recovering the composition of melt and the fluid regime at the onset of

645   crustal anatexis and S-type granite formation. *Geology, 41,* 115-118.

646   Bartoli, O., Cesare, B., Remusat, L., Acosta-Vigil, A., & Poli, S. (2014). The H_2O content of

647   granite embryos. *Earth and Planetary Science Letters*, *395*, 281–290.

648   Bartoli, O., Acosta-Vigil, A., & Cesare, B. (2015). High-temperature metamorphism and

649   crustal melting: working with melt inclusions. *Periodico di Mineralogia*, *84*, 591-614.

650   Bartoli, O., Acosta-Vigil, A., Tajčmanová, L., Cesare, B., & Bodnar, R.J. (2016). Using

651   nanogranitoids and phase equilibria modeling to unravel anatexis in the crustal

652   footwall of the Ronda peridotites (Betic Cordillera, S Spain), *Lithos, 256-257,* 282-

653   299.

654   Behrens, H., & Jantos, N. (2001). The effect of anhydrous composition on water solubility in

655   granitic melts. *American Mineralogist*, *86*, 14-20.

656   Boulard, E., Guyot, F., & Fiquet, G. (2012). The influence on Fe content on Raman spectra and

657   unit cell parameters of magnesite-siderite solid solutions. *Physics and Chemistry of*

658   *Minerals*, *39*, 239-246.

659   Brandt, S., Will, T.M., Klemd, R. (2007). Magmatic loading in the proterozoic Epupa

660   Complex, NW Namibia, as evidenced by ultrahigh-temperature sapphirine-bearing

661   orthopyroxene-sillimanite-quartz granulites. *Precambrian Research, 153*, 143-178.

662   Brooker, R.A., Kohn, S.C., Holloway, J.R., McMillan, P.F., Carroll, M.R. (1999). Solubility,

663   speciation and dissolution mechanisms for CO_2 in melts on the $NaAlO_2$-SiO_2 join.

664   *Geochimica et Cosmochimica Acta*, *63*, 3549-3565.

665   Brown, M., Korhonen, F.J., Siddoway, C.S. (2011). Organizing melt flow through the crust.

666   *Elements, 7,* 261-266.

667 Brown, M., & Johnson, T. (2018). Secular change in metamorphism and the onset of global

668   plate tectonics. *American Mineralogist*, *103*, 181-196.

669 Bucher-Nurminen, K., & Droop, G. (1983). The metamorphic evolution of garnet-cordierite-

670   sillimanite-gneisses oft he Gruf-Complex, Eastern Pennine Alps. *Contributions to*

671   *Mineralogy and Petrology*, *84*, 215-227.

672 Buick, I. S., Stevens, G., & Gibson, R. L. (2004). The role of water retention in the anatexis of

673   metapelites in the Bushveld Complex Aureole, South Africa: an experimental study.

674   *Journal of Petrology*, *45*, 1777-1797.

675 Bureau, H., Trocellier, P., Shaw, C., Khodja, H., Bolfan-Casanova, N., & Demouchy, S.

676   (2003). Determination of the concentration of water dissolved in glasses and minerals

677   using nuclear microprobe. *Nuclear Instruments & Methods in Physics Research,*

678   *Section B: Beam Interactions with Materials and Atoms*, *210*, 449–454.

679 Carvalho, B. B., Sawyer, E. W., & Janasi, V. A. (2016). Crustal reworking in a shear zone:

680   Transformation of metagranite to migmatite. *Journal of Metamorphic Geology*, *34*,

681   237–264.

682 Carvalho, B.B., Bartoli, O., Ferri, F., Cesare, B., Ferrero, S., Remusat, L., Capizzi, L.S. & Poli,

683   S. 2019. Anatexis and fluid regime of the deep continental crust: New clues from melt

684   and fluid inclusions in metapelitic migmatites from Ivrea Zone (NW Italy). *Journal of*

685   *Metamorphic Geology*, *37*, 951-975.

686 Castro, N. A., de Araujo, C. E. G., Basei, M. A., Osako, L. S., Nutman, A. A., & Liu, D. (2012).

687   Ordovician A-type granitoid magmatism on the Ceará Central Domain, Borborema

688   Province, NE-Brazil. *Journal of South American Earth Sciences*, *36*, 18-31.

689 Cesare, B., Marchesi, C., Hermann, J., Gómez-Pugnaire, M.T. (2003). Primary melt

690   inclusions in andalusite from anatectic graphitic metapelites: implications for the

691   position of the Al_2SiO_5 triple point. *Geology, 31*, 573-576.

692   Cesare, B., Maineri, C., Baron Toaldo, A., Pedron, D., Acosta-Vigil, A. (2007). Immiscibility

693   between carbonic fluids and granitic melts during crustal anatexis: a fluid and melt

694   inclusion study in the enclaves of the Neogene Volcanic Province of SE Spain.

695   *Chemical Geology*, *237*, 433-449

696   Cesare, B., Ferrero, S., Salvioli-Mariani, E., Pedron, D., Cavallo, A. (2009). "Nanogranite"

697   and glassy inclusions: The anatectic melt in migmatites and granulites. *Geology, 37,*

698   627-630.

699   Cesare, B., Acosta-Vigil, A., Bartoli, O., & Ferrero, S., (2015). What can we learn from melt

700   inclusions in migmatites and granulites? *Lithos, 239*, 186-216.

701   Chappell, B. W., & White, A. J. R. (1992). I-and S-type granites in the Lachlan Fold Belt.

702   *Earth and Environmental Science Transactions of the Royal Society of Edinburgh*, *83*,

703   1-26.

704   Clemens, J.D., Holloway, J.R., White, A.J.R. (1986). Origin of an A-type granite: experimental

705   constraints. *American Mineralogist, 71,* 317-324.

706   Clemens, J.D., & Stevens, G. (2016). Melt segregation and magma interactions during crustal

707   melting: breaking out of the matrix. *Earth-Science Reviews, 160,* 333-349.

708   Clemens, J.D., & Watkins, J. M. (2001). The fluid regime of high-temperature metamorphism

709   during granitoid magma genesis. *Contributions to Mineralogy and Petrology*, *140*, 600-

710   606.

711   Connolly, J. A., & Podladchikov, Y. Y. (2015). An analytical solution for solitary porosity

712   waves: dynamic permeability and fluidization of nonlinear viscous and viscoplastic

713   rock. *Geofluids*, *15*, 269-292.

714   Créon, L., Levresse, G., Remusat, L., Bureau, H., & Carrasco-Núñez, G. (2018). New method

715   for initial composition determination of crystallized silicate melt inclusions. *Chemical*

716   *Geology*, *483*, 162–173.

717 de Almeida, C. N., de Pinho Guimarães, I., & da Silva Filho, A. F. (2002). A-type post-

718   collisional granites in the Borborema province-NE Brazil: The Queimadas pluton.

719   *Gondwana Research*, *5*, 667-681.

720 Droop, G. R., & Bucher-Nurminen, K. (1984). Reaction textures and metamorphic evolution

721   of sapphirine-bearing granulites from the Gruf Complex, Italian Central Alps. *Journal*

722   *of Petrology*, *25*, 766-803.

723 Droop, G. T. R., Clemens, J. D., & Dalrymple, D. J. (2003). Processes and conditions during

724   contact anatexis, melt escape and restite formation: the Huntly Gabbro Complex, NE

725   Scotland. *Journal of Petrology*, *44*, 995-1029.

726 Dubessy, J., Poty, B., & Ramboz, C. (1989). Advances in C-O-H-N-S fluid geochemistry based

727   on micro-Raman spectrometric analysis of fluid inclusions. *European Journal of*

728   *Mineralogy*, *1*, 517-534.

729 Esposito, R., Lamadrid, H. M., Redi, D., Steele-MacInnis, M., Bodnar, R. J., Manning, C. E.,

730   De Vivo, B., Cannatelli, C., & Lima, A. (2016). Detection of liquid H_2O in vapor

731   bubbles in reheated melt inclusions: Implications for magmatic fluid composition and

732   volatile budgets of magmas? *American Mineralogist*, *101*, 1691-1695.

733 Ferrero, S., Bartoli, O., Cesare, B., Salvioli-Mariani, E., Acosta-Vigil, A., Cavallo, A.,

734   Groppo, C., Battiston, S. (2012). Microstructures of melt inclusions in anatectic

735   metasedimentary rocks. *Journal of Metamorphic Geology, 30,* 303-322.

736 Ferrero, S., Braga, R., Berkesi, M., Cesare, B., & Laridhi Ouazaa, N. (2014). Production of

737   metaluminous melt during fluid-present anatexis: an example from the Maghrebian

738   basement, La Galite Archipelago, central Mediterranean. *Journal of Metamorphic*

739   *Geology*, *32*, 209-225.

740   Ferrero, S., Wunder, B., Walczak, K., O'Brien, P.J., Ziemann, M.A. (2015). Preserved near

741   ultrahigh-pressure melt from continental crust subducted to mantle depths.

742   *Geology, 43,* 447-450.

743   Florisbal, L. M., de Fátima Bitencourt, M., Nardi, L. V. S., & Conceição, R. V. (2009). Early

744   post-collisional granitic and coeval mafic magmatism of medium-to high-K tholeiitic

745   affinity within the Neoproterozoic Southern Brazilian Shear Belt. *Precambrian*

746   *Research*, *175*, 135-148.

747   Galli A., Le Bayon B., Schmidt M.W., Burg J.-P., Caddick M.J., Reusser E. (2011).

748   Granulites and charnockites of the Gruf Complex: Evidence for Permian ultra-high

749   temperature metamorphism in the Central Alps. *Lithos*, *124*, 17-45.

750   Galli, A., Le Bayon, B., Schmidt, M.W., Burg, J.-P., Reusser, E., Sergeev, S.A., Larionov, A.

751   (2012). U-Pb zircon dating of the Gruf Complex: disclosing the late Variscan granulitic

752   lower crust of Europe stranded in the Central Alps. *Contributions to Mineralogy and*

753   *Petrology, 163*, 353-378.

754   Galli, A., Le Bayon, B., Schmidt, M. W., Burg, J. P., & Reusser, E. (2013).

755   Tectonometamorphic history of the Gruf complex (Central Alps): exhumation of a

756   granulite–migmatite complex with the Bergell pluton. *Swiss Journal of Geosciences*,

757   *106*, 33-62.

758   Ganguly, J., Dasgupta, S., Cheng, W., & Neogi, S. (2000). Exhumation history of a section of

759   the Sikkim Himalayas, India: records in the metamorphic mineral equilibria and

760   compositional zoning of garnet. *Earth and Planetary Science Letters*, *183*, 471- 486.

761   Gerya, T. V., Perchuk, L. L., Maresch, W. V., & Willner, A. P. (2004). Inherent gravitational

762   instability of hot continental crust: Implications for doming and diapirism in granulite

763   facies terrains. *Special paper - Geological Society of America*, *380*, 97-116.

764 Gerya, T. V., Perchuk, L. L., & Burg, J. P. (2008). Transient hot channels: perpetrating and

765 regurgitating ultrahigh-pressure, high-temperature crust–mantle associations in

766 collision belts. *Lithos*, *103*, 236-256.

767 Ghani, A. A., Hazad, F. I., Jamil, A., Xiang, Q. L., Ismail, W. N. A. W., Chung, S. L., ... &

768 Mohd, M.R. (2014). Permian ultrafelsic A-type granite from Besar Islands group,

769 Johor, peninsular Malaysia. *Journal of Earth System Science*, *123*, 1857-1878.

770 Gianola, O., Schmidt, M.W., von Quadt, A., Peytcheva, I., Luraschi, P., Reusser, E. (2014).

771 Continuity in geochemistry and time of the Tertiary Bergell intrusion (Central Alps).

772 *Swiss Journal of Geosciences*, *107*, 197-222.

773 Giordano, D., Russell, J. K., & Dingwell, D. B. (2008). Viscosity of magmatic liquids: a model.

774 *Earth and Planetary Science Letters*, *271*, 123-134.

775 Goodenough, K. M., Upton, B. G. J., & Ellam, R. M. (2000). Geochemical evolution of the

776 Ivigtut granite, South Greenland: a fluorine-rich "A-type" intrusion. *Lithos*, *51*, 205-

777 221.

778 Grant, J.A. (2009). THERMOCALC and experimental modelling of melting of pelite, Morton

779 Pass, Wyoming. *Journal of metamorphic geology, 27,* 571-578.

780 Hacker, B. R., Kelemen, P. B., & Behn, M. D. (2015). Continental lower crust. *Annual Review*

781 *of Earth and Planetary Sciences*, *43*, 167-205.

782 Harley, S.L., Hensen, B.J., Sheraton, J.W. (1990). Two-stage decompression in orthopyroxene

783 –sillimanite granulites from Forefinger Point, Enderby Land, Antarctica: implications

784 for the evolution of the Archean Napier Complex. *Journal of metamorphic geology, 8,*

785 591-613.

786 Harley, S. L. (1998). On the occurrence and characterization of ultrahigh-temperature crustal

787 metamorphism. In: Treloar, P.J., O'Brian, P.J. (Eds.), What drives metamorphism and

788 metamorphic reactions? *Geological Society, London, Special Publications*, *138*, 81-107

789   Harley, S.L. (2008). Refining the P-T records of UHT crustal metamorphism. *Journal of*
790   *metamorphic geology, 26,* 125-154.

791   Hermann, J., & Spandler, C.J. (2008). Sediment melts at sub-arc depths: an experimental study.
792   *Journal of Petrology*, *49*, 717-740.

793   Hoefs, J., & Touret, J. (1975). Fluid inclusion and carbon isotope study from Bamble granulites
794   (South Norway). *Contributions to Mineralogy and Petrology*, *52*, 165-174.

795   Holland, T., & Powell, R. (2001). Calculation of phase relations involving haplogranitic melts
796   using an internally consistent thermodynamic dataset. *Journal of Petrology, 42,* 673-
797   683.

798   Holness, M. B., & Sawyer, E. W. (2008). On the pseudomorphing of melt-filled pores during
799   the crystallization of migmatites. *Journal of Petrology*, *49*, 1343-1363.

800   Holtz, F., Johannes, W., Tamic, N., & Behrens, H. (2001). Maximum and minimum water
801   contents of granitic melts generated in the crust: a reevaluation and implications. *Lithos*,
802   *56*, 1-14.

803   Iacovino, K., & Till, C. B. (2019). DensityX: A program for calculating the densities of
804   magmatic liquids up to 1,627° C and 30 kbar. *Volcanica*, *2*, 1-10.

805   Jackson, D. H., Mattey, D. P., & Harris, N. B. W. (1988). Carbon isotope compositions of fluid
806   inclusions in charnockites from southern India. *Nature*, *333*, 167.

807   Jamieson, R.A., Unsworth, M.J., Harris, N.B.W., Rosenberg, C.L., Schulmann, K. (2011).
808   Crustal melting and the flow of mountains. *Elements, 7,* 253-260.

809   Johannes, W., & Holtz, F. (1996). Petrogenesis and experimental petrology of granitic rocks.
810   Berlin Heidelberg: Springer-Verlag.

811   Jung, S., Hoernes, S., & Mezger, K. (2000). Geochronology and petrogenesis of Pan-African,
812   syn-tectonic, S-type and post-tectonic A-type granite (Namibia): products of melting of

crustal sources, fractional crystallization and wall rock entrainment. *Lithos*, *50*, 259-287.

Kalsbeek, F., Jepsen, H. F., & Jones, K. A. (2001). Geochemistry and petrogenesis of S-type granites in the East Greenland Caledonides. *Lithos*, *57*, 91-109.

Kelsey, D.E. (2008). On ultrahigh-temperature crustal metamorphism. *Gondwana Research, 13,* 1-29.

Kelsey, D.E., Hand, M. (2015). On ultrahigh temperature crustal metamorphism: phase equilibria, trace element thermometry, bulk composition, heat sources, timescales and tectonic settings. *Geoscience Frontiers, 6,* 311-356.

King, P. L., White, A. J. R., Chappell, B. W., & Allen, C. M. (1997). Characterization and origin of aluminous A-type granites from the Lachlan Fold Belt, southeastern Australia. *Journal of Petrology*, *38*, 371-391.

King, P. L., Chappell, B. W., Allen, C. M., & White, A. J. R. (2001). Are A-type granites the high-temperature felsic granites? Evidence from fractionated granites of the Wangrah Suite. *Australian Journal of Earth Sciences*, *48*, 501-514.

Lamadrid, H. M., Lamb, W. M., Santosh, M., & Bodnar, R. J. (2014). Raman spectroscopic characterization of H_2O in CO_2-rich fluid inclusions in granulite facies metamorphic rocks. *Gondwana Research*, *26*, 301-310.

Le Breton, N., Thompson, A.B. (1988). Fluid-absent (dehydration) melting of biotite in metapelites in the early stages of crustal anatexis. *Contributions to Mineralogy and Petrology, 99,* 226-237.

Liati, A., Gebauer, D., & Fanning, M. (2000). U-Pb SHRIMP dating of zircon from the Novate granite (Bergell, Central Alps): evidence for Oligocene-Miocene magmatism, Jurassic/Cretaceous continental rifting and opening of the Valais trough. *Schweizerische Mineralogische und Petrographische Mitteilungen*, *80*, 305-316.

838   Lowenstern, J. B. (1995). Applications of silicate-melt inclusions to the study of magmatic

839   volatiles. *Magmas, Fluids, and Ore Deposits*, *23*, 71–99.

840   Marchildon, N., Brown M. (2001). Melt segregation in late syn-tectonic anatectic migmatites:

841   an example from the Onawa contact aureole, Maine, USA. *Physics and Chemistry of*

842   *the Earth, Part A: Solid Earth and Geodesy, 26,* 225-229.

843   McDermott, F., Harris, N. B. W., & Hawkesworth, C. J. (2000). Geochemical constraints on

844   the petrogenesis of Pan-African A-type granites in the Damara Belt, Namibia. *Henno*

845   *Martin Commemorative Volume: Communications of the Geological Survey of*

846   *Namibia, Special Publication of the Geol. Survey of Namibia*, *12*, 139-148.

847   Milord, I., Sawyer, E.W., Brown, M. (2001). Formation of diatexite migmatite and granite

848   magma during anatexis of semi-pelitic metasedimentary rocks: an example from St.

849   Malo, France. *Journal of Petrology, 42,* 487-505.

850   Moin, B., Guillot, C., & Gibert, F. (1994). Controls of the composition of nitrogen-rich fluids

851   originating from reaction with graphite and ammonium-bearing biotite. *Geochimica et*

852   *Cosmochimica Acta*, *58*, 5503-5523.

853   Montel, J-M., Vielzeuf, D. (1997). Partial melting of metagreywackes, part II. Compositions

854   of minerals and melts. *Contributions to Mineralogy and Petrology, 128,* 176-196.

855   Morgan, G. B., & London, D. (2005). Effect of current density on the electron microprobe

856   analysis of alkali aluminosilicate glasses. *American Mineralogist*, *90*, 1131-1138.

857   Nagel, T., De Capitani, C., Frey, M. (2002). Isograds and P-T evolution in the eastern

858   Lepontine Alps (Graubünden, Switzerland). *Journal of Metamorphic Geology*, *20*, 309-

859   324.

860   Nandakumar, V., & Harley, S. L. (2000). A reappraisal of the pressure-temperature path of

861   granulites from the Kerala Khondalite Belt, southern India. *The Journal of Geology*,

862   *108*, 687-703.

Ni, H., Keppler, H. (2013). Carbon in silicate melts. *Reviews in Mineralogy & Geochemistry*, *75*, 251-287.

Oberli, F., Meier, M., Berger, A., Rosenberg, C.L., & Gieré, R. (2004). U-Th-Pb and ^{230}Th/^{238}U disequilibrium isotope systematics: Precise accessory mineral chronology and melt evolution tracing in the Alpine Bergell intrusion. *Geochimica et Cosmochimica Acta*, *68*, 2543-2560.

Patiño Douce, A. E., & Johnston, A. D. (1991). Phase equilibria and melt productivity in the pelitic system: implications for the origin of peraluminous granitoids and aluminous granulites. *Contributions to Mineralogy and Petrology*, *107*, 202-218.

Rosenberg, C. L., & Handy, M. R. (2005). Experimental deformation of partially melted granite revisited: implications for the continental crust. *Journal of metamorphic Geology*, *23*, 19-28.

Samperton, K.M., Schoene, B., Cottle, J.M., Keller, C.B., Crowley, J.L., Schmitz, M.D. (2015). Magma emplacement, differentiation and cooling in the middle crust: integrated zircon geochronological-geochemical constraints from the Bergell intrusion, Central Alps. *Chemical Geology*, *417*, 322-340.

Santosh, M., Tsunogae, T., Li, J.H., Liu, S.J. (2007). Discovery of sapphirine-bearing Mg-Al granulites in the North China Craton: implications for Paleoproterozoic ultrahigh temperature metamorphism. *Gondwana Research*, *11*, 263-285.

Santosh, M., & Omori, S. (2008). CO_2 flushing: a plate tectonic perspective. *Gondwana Research*, *13*, 86-102.

Sawyer, E.W. (1994). Melt segregation in the continental crust. *Geology*, *22*, 1019-1022.

Sawyer, E.W. (2008). *Atlas of migmatites*. The Canadian Mineralogist Special Publication 9. Quebec: Mineralogical Association of Canada; Ottawa: NRC Research Press.

887   Sawyer, E.W., Cesare, B., Brown M. (2011). When the continental crust melts. *Elements, 7,*
888   229-234.

889   Scaillet, B., Holtz, F., Pichavant, M., & Schmidt, M. (1996). Viscosity of Himalayan
890   leucogranites: Implications for mechanisms of granitic magma ascent. *Journal of*
891   *Geophysical Research: Solid Earth*, *101*, 27691-27699.

892   Schmidt, M. W. (2015). Melting of pelitic sediments at subarc depths: 2. Melt chemistry,
893   viscosities and a parameterization of melt composition. *Chemical Geology*, *404*, 168-
894   182.

895   Stevens, G., Clemens, J.D., Droop, G.T.R. (1997). Melt production during granulite-facies
896   anatexis: experimental data from "primitive" metasedimentary protoliths.
897   *Contributions to Mineralogy and Petrology, 128,* 352-370.

898   Stevens, G., Villaros, A., Moyen, J-F. (2007). Selective peritectic garnet entrainment as the
899   origin of geochemical diversity in S-type granites. *Geology, 35,* 9-12.

900   Rudnick, R.L. (1995). Making continental crust. *Nature, 378,* 571-578.

901   Tacchetto, T., Bartoli, O., Cesare, B., Berkesi, M., Aradi, L. E., Dumond, G., & Szabó, C.
902   (2019). Multiphase inclusions in peritectic garnet from granulites of the Athabasca
903   granulite terrane (Canada): Evidence of carbon recycling during Neoarchean crustal
904   melting. *Chemical Geology*, *508*, 197-209.

905   Tamic, N., Behrens, H., & Holtz, F. (2001). The solubility of H_2O and CO_2 in rhyolitic melts
906   in equilibrium with a mixed CO_2–H_2O fluid phase. *Chemical geology*, *174*, 333-347.

907   Taylor, S.R., McLennan, S.M. (1995). The geochemical evolution of the continental crust.
908   *Reviews of Geophysics*, *33*, 241-265.

909   Teyssier, C., & Whitney, D. L. (2002). Gneiss domes and orogeny. *Geology*, *30*, 1139-1142.

910

911 Thomen, A., Robert, F., & Remusat, L. (2014). Determination of the nitrogen abundance in

912   organic materials by NanoSIMS quantitative imaging. *Journal of Analytical Atomic*

913   *Spectrometry*, *29*, 512–519.

914 Todd, C.S., Engi, M. (1997). Metamorphic field gradients in the Central Alps. *Journal of*

915   *metamorphic geology*, *15*, 513-530.

916 Touret, J. L., & Huizenga, J. M. (2011). Fluids in granulites. *Geological Society of America*

917   *Memoirs*, *207*, 25-37.

918 Trommsdorff, V., & Nievergelt, P. (1983). The Bregaglia (Bergell) Iorio intrusive and its field

919   relations. *Memorie della Società Geologica Italiana*, *26*, 55-68.

920 Tulloch, A. J., Ramezani, J., Kimbrough, D. L., Faure, K., & Allibone, A. H. (2009). U-Pb

921   geochronology of mid-Paleozoic plutonism in western New Zealand: Implications for

922   S-type granite generation and growth of the east Gondwana margin. *Geological Society*

923   *of America Bulletin*, *121*, 1236-1261.

924 Turcotte, D., & Schubert, G. (2014). Geodynamics. Cambridge university press.

925 Vielzeuf, D., Holloway, J.R. (1988). Experimental determination of the fluid-absent melting

926   relations in the pelitic system. *Contributions to Mineralogy and Petrology, 98,* 257-

927   276.

928 Vigneresse, J. L., Barbey, P., & Cuney, M. (1996). Rheological transitions during partial

929   melting and crystallization with application to felsic magma segregation and transfer.

930   *Journal of Petrology*, *37*, 1579-1600.

931 Visonà, D., & Lombardo, B. (2002). Two-mica and tourmaline leucogranites from the Everest–

932   Makalu region (Nepal–Tibet). Himalayan leucogranite genesis by isobaric heating?

933   *Lithos*, *62*, 125-150.

934 Von Blanckenburg, F. (1992). Combined high-precision chronometry and geochemical

935   tracing using accessory minerals: Applied to the Central-Alpine Bergell intrusion

936 (Central Europe). *Chemical Geology*, *100*, 19-40.

937 Von Blanckenburg, F., Früh-Green, G., Diethelm, K., & Stille, P. (1992). Nd-, Sr-, O-

938 isotopic and chemical evidence for a two-stage contamination history of mantle magma

939 in the Central-Alpine Bergell intrusion. *Contributions to Mineralogy and Petrology*,

940 *110*, 33-45.

941 Wang, X., Ming Chou, I., Hu, W., Burruss, R.C., Sun, Q., & Song Y. (2011). Raman

942 spectroscopic measurements of CO_2 density: experimental calibration with high-

943 pressure optical cell (HPOC) and fused silica capillary capsule (FSCC) with application

944 to fluid inclusion observations. *Geochimica et Cosmochimica Acta*, *75*, 4080-4093.

945 Wenk, E., (1955). Eine Strukturkarte der Tessineralpen. *Schweizerische und Mineralogische*

946 *und Petrographische Mitteilungen*, *35*, 311-319.

947 Whalen, J. B., Currie, K. L., & Chappell, B. W. (1987). A-type granites: geochemical

948 characteristics, discrimination and petrogenesis. *Contributions to Mineralogy and*

949 *Petrology*, *95*, 407-419.

950 White, R.W., Powell, R. (2002). Melt loss and the preservation of granulite facies material

951 assemblages. *Journal of metamorphic geology, 20,* 621-632.

952 White, R.W., Stevens, G., Johnson, T.E. (2011). Is the crucible reproducible? Reconciling

953 melting experiments with thermodynamic calculations. *Elements, 7*, 241-246.

954 Whitney, D. L., Teyssier, C., & Fayon, A. K. (2004). Isothermal decompression, partial melting

955 and exhumation of deep continental crust. *Geological Society, London, Special*

956 *Publications*, *227*, 313-326.

957 Yu, B., Santosh, M., Li, S. S., & Shaji, E. (2019). Petrology, phase equilibria modelling, and

958 in situ zircon and monazite geochronology of ultrahigh-temperature granulites from the

959 khondalite belt of southern India. *Lithos*, *348-349*, 105195.

960   Zhang, H. F., Parrish, R., Zhang, L., Xu, W. C., Yuan, H. L., Gao, S., & Crowley, Q. G. (2007).

961   A-type granite and adakitic magmatism association in Songpan–Garze fold belt, eastern

962   Tibetan Plateau: implication for lithospheric delamination. *Lithos*, *97*, 323-335.

963

964

965

966

967

968

969

970

971

972

973

974

975

976

977

978

979

980

981

982

983

984

	Type A granulites		Type C granulites	
	BRE-core	BRE-rim (glassy)	GRAG-core	GRAG-rim
No. analyses by EPMA[a] / NanoSIMS	6 / 6	11	21 / 3	6 / 7
Wt%				
SiO_2	70.08 (2.51)	75.33 (1.26)	74.90 (1.00)	71.93 (1.54)
TiO_2	0.05 (0.04)	0.00 (0.01)	0.05 (0.04)	0.06 (0.07)
Al_2O_3	14.45 (0.88)	12.87 (0.64)	11.75 (0.43)	13.29 (1.19)
FeO	1.67 (0.32)	0.91 (0.05)	1.52 (0.14)	1.93 (0.36)
MnO	0.05 (0.02)	0.05 (0.02)	0.02 (0.02)	0.08 (0.04)
MgO	0.54 (0.24)	0.10 (0.08)	0.71 (0.10)	0.53 (0.23)
CaO	0.94 (0.55)	0.05 (0.02)	0.51 (0.15)	0.55 (0.19)
Na_2O	1.96 (0.54)	1.66 (0.38)	0.73 (0.27)	0.72 (0.39)
K_2O	7.31 (1.43)	8.67 (0.82)	6.96 (0.48)	7.95 (1.88)
P_2O_5	0.20 (0.18)	0.04 (0.03)	0.12 (0.06)	0.17 (0.15)
Cl	0.04 (0.03)	0.01 (0.00)	0.06 (0.02)	0.12 (0.04)
Total	97.31 (2.33)	99.70 (0.31)	97.33 (0.79)	97.33 (1.57)
H_2O by NanoSIMS [wt%]	6.20 (1.25)	-	7.05 (3.00)	4.35 (0.92)
CO_2 by NanoSIMS [ppm]	779 (326)	-	1113 (843)	940 (407)
ASI	1.14 (0.13)	1.06 (0.03)	1.24 (0.07)	1.27 (0.19)
K#	71 (8)	77 (5)	87 (4)	87 (7)
Mg#	35 (8)	13 (8)	44 (4)	32 (11)
CIPW norm				
Quartz	27.04	31.56	40.98	34.15
Corundum	2.10	0.76	2.39	2.89
Orthoclase	43.23	51.23	41.13	46.98
Albite	16.59	14.02	6.16	6.13
Anorthite	3.31	0.00	1.73	1.65
Hypersthene	4.43	2.01	4.51	4.91
Ilmenite	0.10	0.01	0.09	0.11
Apatite	0.47	0.10	0.29	0.39

[a] EPMA = electron probe micro-analyzer

985

986 **TABLE 1** Average compositions of remelted and preserved glassy MI. Numbers in parentheses

987 refer to the standard error of the mean expressed as 2σ. ASI = molar

988 $[Al_2O_3/(CaO+Na_2O+K_2O)]$, K# = molar $[K_2O/(K_2O+Na_2O)]$ x 100; Mg# = molar

989 $[MgO/(MgO+FeO)]$ x 100.

Analysis	Sample	Approx. size	Homogeneity	H$_2$O [wt%]	1σ error	CO$_2$ [ppm]	1σ error
Type A granulites							
C_MI1_Gr1	BRE17-B13 core	<10 µm	Glass	5.52	0.04	460	20
C_MI3_Gr3_1	BRE17-B13 core	≥ 20 µm	Glass + bubble	8.27	0.27	1164	33
C_MI3_Gr3_2	BRE17-B13 core	≥ 20 µm	Glass + bubble	7.34	0.23	1064	31
C_MI16_Gr4	BRE17-B13 core	≥ 20 µm	Glass + 10% crystals + bubble	6.88	0.21	1194	34
E_MI6_Gr2_1	BRE17-D2 core	<10 µm	Glass	4.41	0.04	408	17
E_MI6_Gr2_2	BRE17-D2 core	<10 µm	Glass	4.76	0.04	387	17
OG16_MI2_Gr1	BRE17-B13 rim	<10 µm	Glass + 3% crystals	4.68	0.04	1153	32
Type C granulites							
A_MI1_Gr1	GRAG-P3 core	<10 µm	Glass	8.75	0.07	1738	41
A_MI3_Gr2	GRAG-P3 core	<10 µm	Glass + bubble	8.34	0.06	1291	33
A_MI2_Gr2	GRAG-P3 core	<10 µm	Glass + 3% crystals	4.06	0.04	310	17
F_MI12_Gr1	GRAG-P2 Gr1 rim	10 - 20 µm	Glass + 3% crystals	4.51	0.04	160	15
F_MI1_Gr4	GRAG-P2 Gr1 rim	<10 µm	Glass + 2% crystals	2.88	0.04	1569	34
OG18_MI1_Gr4	GRAG-P3 rim	<10 µm	Glass	3.11	0.04	1149	28
OG18_MI3_Gr4	GRAG-P3 rim	<10 µm	Glass	3.44	0.04	1064	32
OG18_MI6_Gr1	GRAG-P3 rim	<10 µm	Glass + 1% crystals	5.18	0.04	221	15
OG18_MI4_Gr2_1	GRAG-P3 rim	10 - 20 µm	Glass	5.94	0.04	1287	31
OG18_MI4_Gr2_2	GRAG-P3 rim	10 - 20 µm	Glass	5.41	0.04	1132	27

990

991 **TABLE 2** H$_2$O and CO$_2$ contents of re-homogenized MI determined by NanoSIMS.

992

993

994

995

996

997

998

999

1000

1001

1   **FIGURES TEXT**
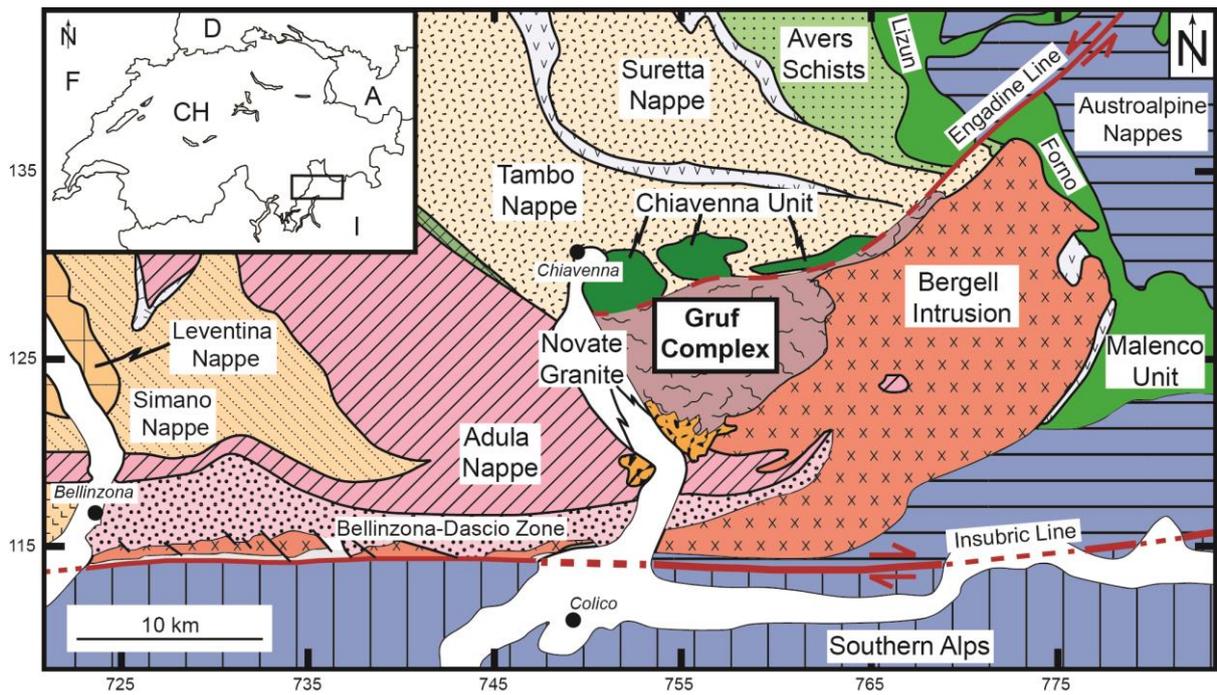
3   **FIGURE 1** Tectonic map of the Central Alps modified after Trommsdorff and Nievergelt

4   (1983). Coordinates are given according to the Swiss geographical grid (units in kilometres).

5

6

7

8

9

10

11

12

13

14

15

16
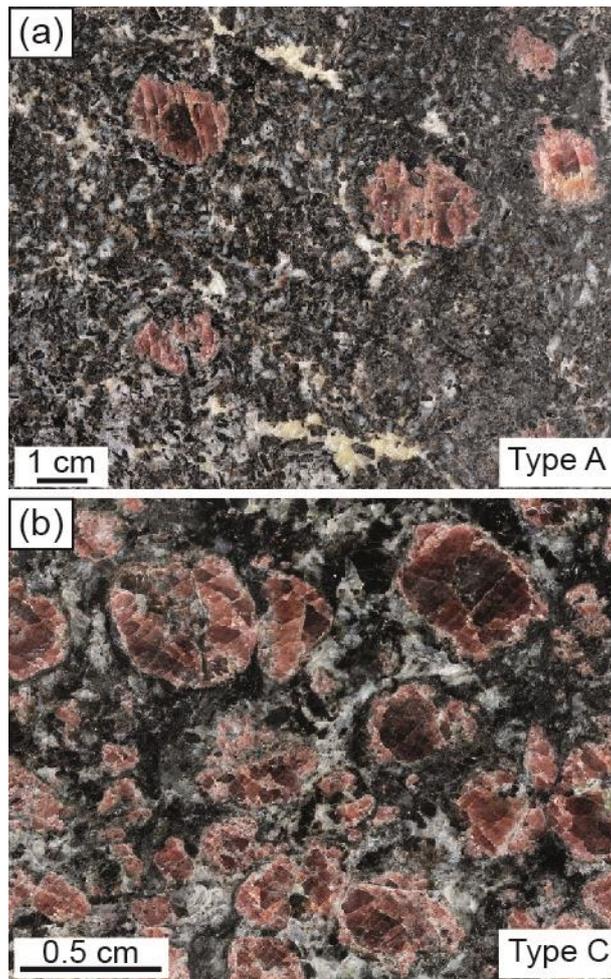
FIGURE 2 UHT granulites from the Gruf Complex. (a) Massive sapphirine-orthopyroxene-cordierite-garnet granulite (Type A) and (b) massive orthopyroxene-cordierite-garnet granulite (Type C).
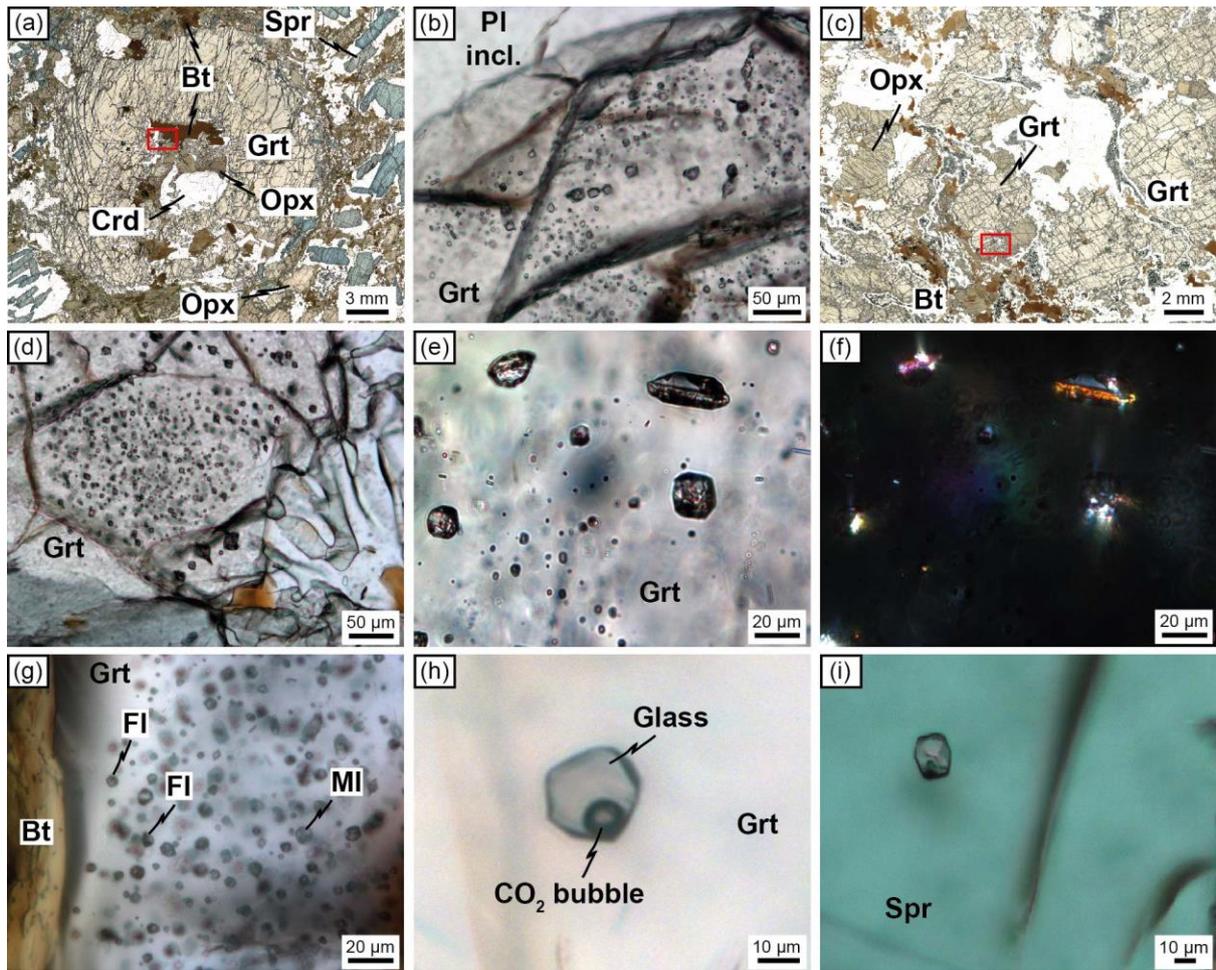
FIGURE 3 Photomicrographs of the granulites from the Gruf Complex. (a) Garnet porphyroblast from a Type A granulite showing a cluster of MI near to the core of the crystal (red box). (b) Zoom of the same cluster of MI as in (a). (c) Garnet porphyroblasts from a Type C granulite. The red box at the rim of the garnet indicate a cluster of MI. (d) Zoom of the same cluster of MI as in (c). (d) Plane-polarized light photomicrograph of MI in garnet. (e) Same as (d) under crossed-polarized light, showing multiple birefringent phases within the inclusions. (g) Fluid inclusions (FI) and MI within a cluster. (h) Glassy MI containing a CO_2 shrinkage bubble. (i) MI in a sapphirine porphyroblast from a Type A granulite.

34
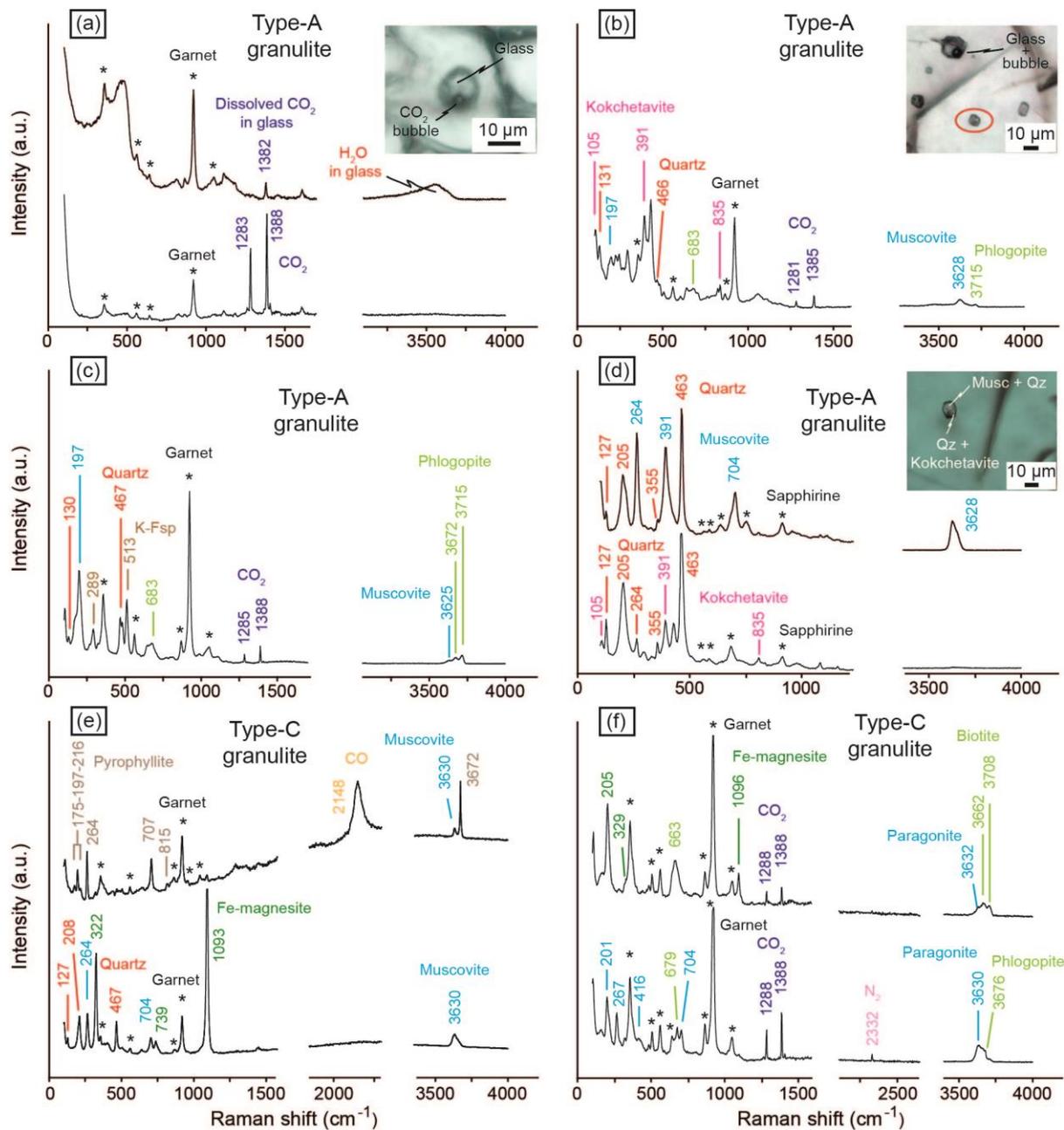
FIGURE 4 Raman spectra of nanogranitoids and glassy MI. (a) Glassy MI with a shrinkage bubble containing CO_2. (b) Analysis of a nanogranitoid inclusion (red circle) close to a glassy MI showing a shrinkage bubble. (c) Nanogranitoid with a CO_2 bubble. (d) Nanogranitoid in sapphirine. (e) Mixed inclusion (fluid + melt) showing CO together with phyllosilicates, quartz and Fe-magnesite. (f) Mixed inclusion with phyllosilicates, Fe-magnesite, CO_2 and N_2.
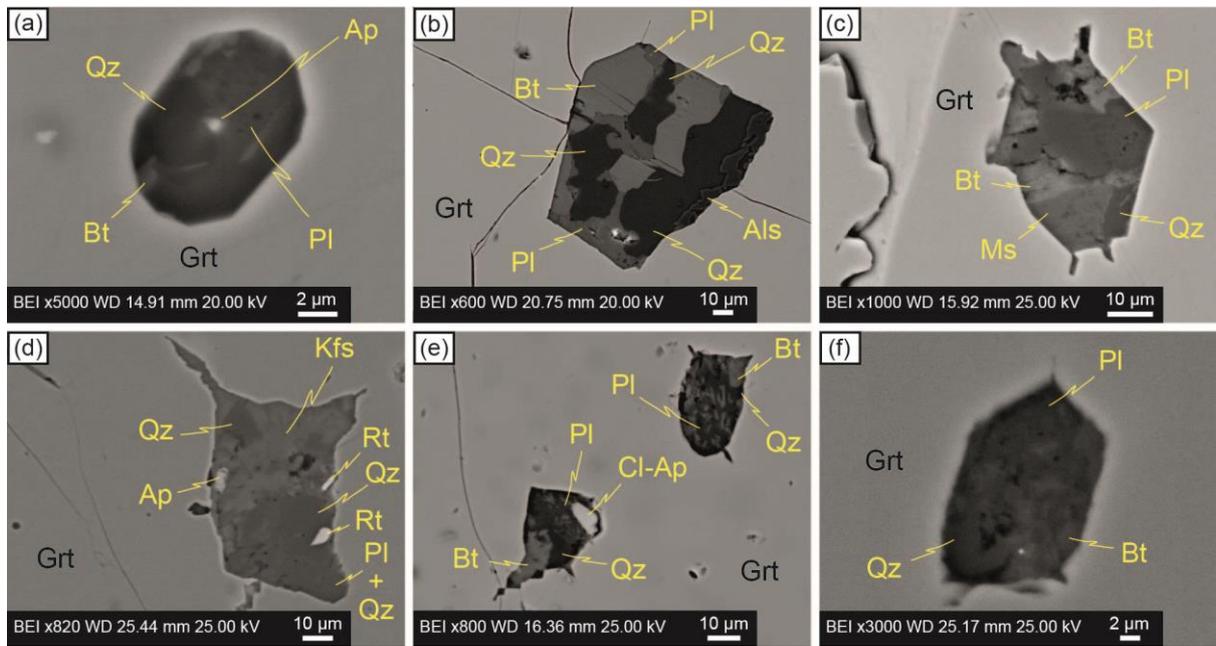
FIGURE 5 Backscattered images of nanogranitoids. Nanogranitoids from Type A (a-d) and from Type C (e-f) granulites are shown.
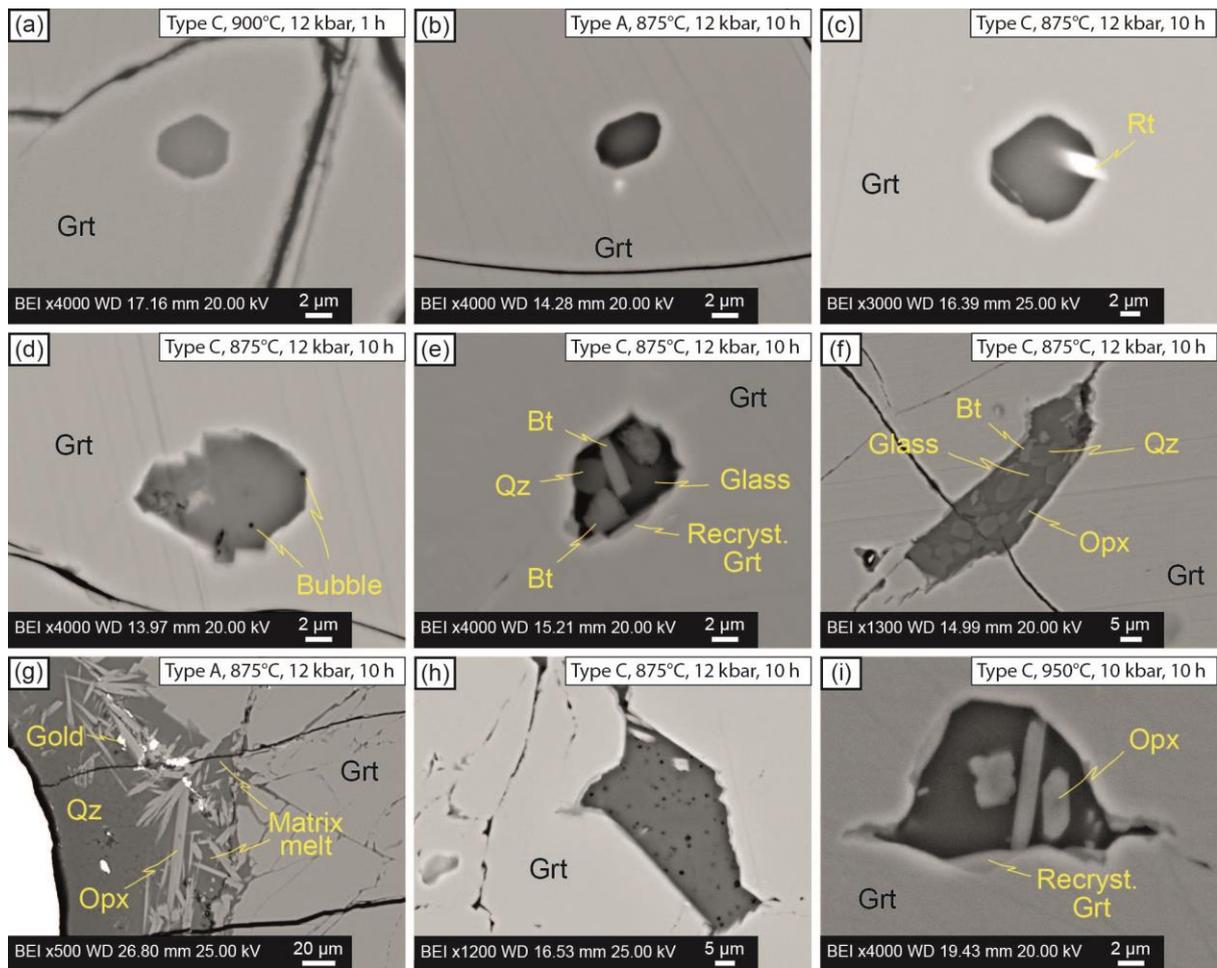
FIGURE 6 Backscattered images of experimentally remelted nanogranitoids. (a,b) Remelted MI with a well-developed negative shape. (c) Re-homogenized MI showing a trapped rutile needle, indenting the wall of the inclusion. (d) MI showing an irregular border and bubbles within the glass. (e,f) Partially remelted nanogranitoids, displaying daughter phases (biotite and quartz) and evidence of minor overheating (recrystallization of garnet and peritectic orthopyroxene). (g) Interaction of matrix melt with a garnet chip, forming peritectic orthopyroxene needles. (h) Melt pocket of infiltrated matrix melt within the garnet chip. The glass displays abundant bubbles. (i) MI from an experiment at 950 °C showing strong evidence of overheating (formation of peritectic orthopyroxene and recrystallization of new garnet at the wall of the inclusion).

71
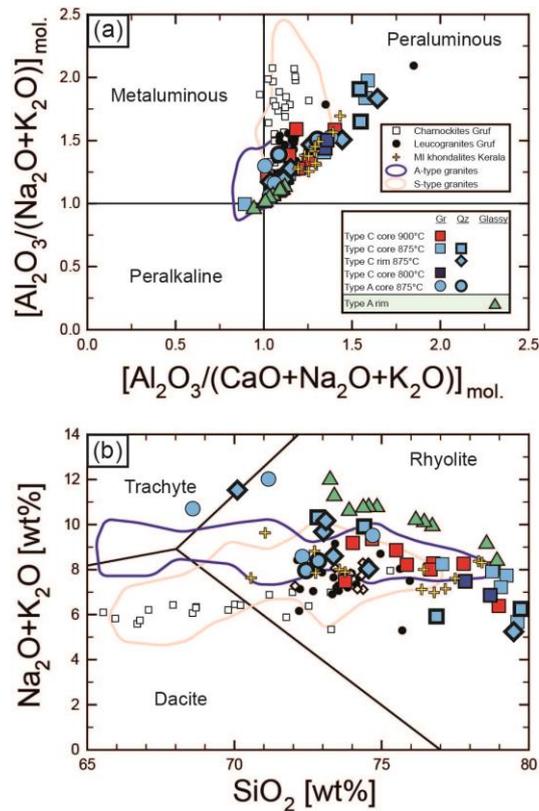
FIGURE 7 Chemical classification of remelted and glassy MI from the Gruf Complex

(normalized to 100% on anhydrous basis). Reported are MI analyses of re-melting

experiments between 800 and 900 °C with graphite-bearing (Gr) and quartz-bearing (Qz)

capsules. (a) Aluminum saturation index vs. alkalinity index. (b) TAS diagram. Analyses for

charnockites and leucogranites from the Gruf Complex are from Galli et al. (2013), whereas

MI analyses from the Kerala Khondalite Belt are from Cesare et al. (2009) and Ferrero et al.

(2012). Data for S-type granites (Chappel & White, 1992; Jung, Hoernes, & Mezger, 2000;

Kalsbeek, Jepsen, & Jones, 2001; Tulloch, Ramezani, Kimbrough, Faure, & Allibone, 2009;

Visonà & Lombardo, 2002) and for A-type granites (Castro et al., 2012; de Almeida, de

Pinho Guimarães, & da Silva Filho, 2002; Florisbal, de Fátima Bitencourt, Nardi, &

Conceição, 2009; Ghani et al., 2014; Goodenough, Upton, & Ellam, 2000; King, White,

Chappell, & Allen, 1997; King, Chappell, Allen, & White, 2001; McDermott, Harris, &

Hawkesworth, 2000; Whalen, Currie, & Chappell, 1987; Zhang et al., 2007) are also reported

for comparison.
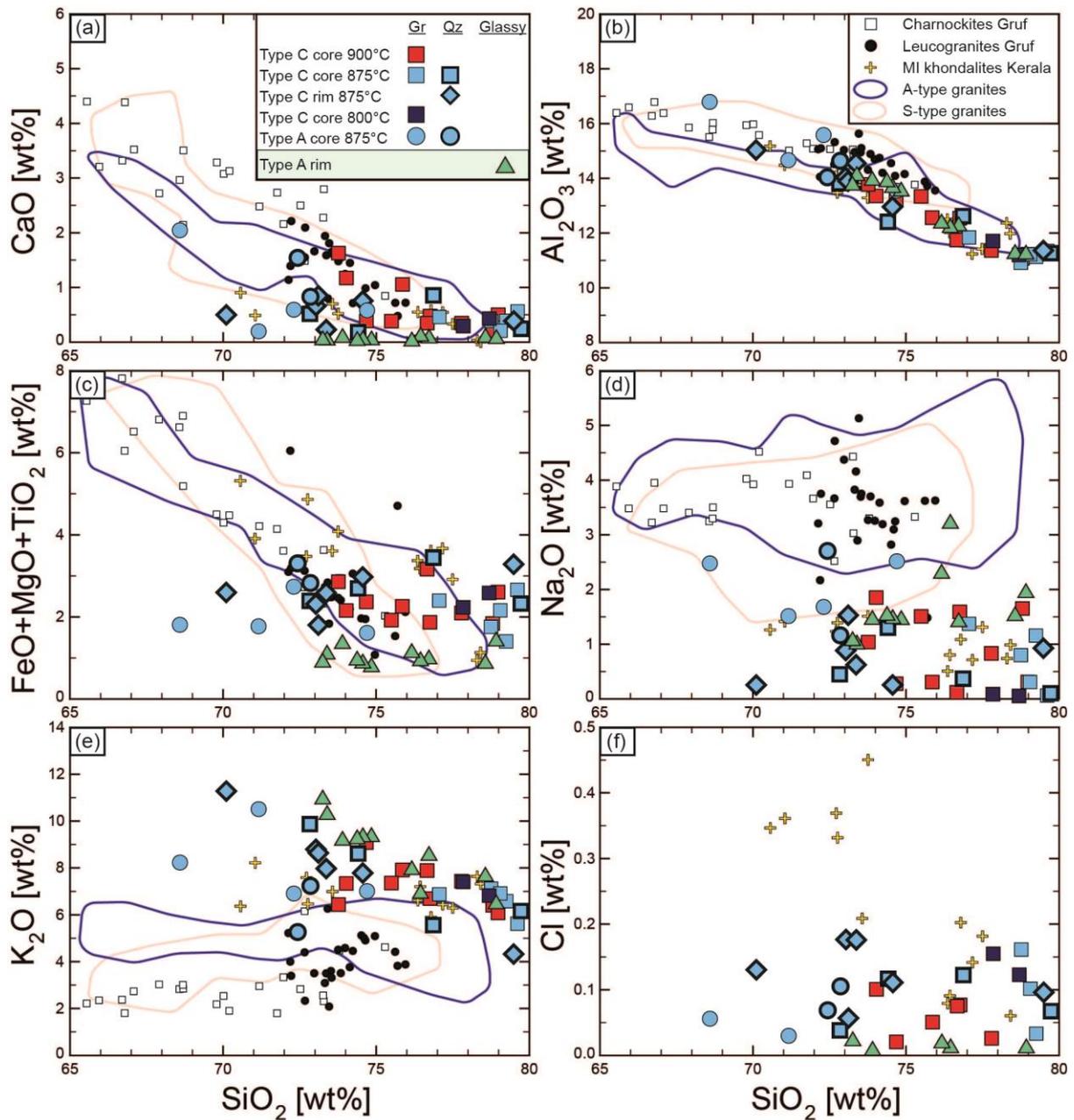
FIGURE 8 Chemical composition of glasses from experimentally remelted and natural glassy inclusions (normalized to 100% on anhydrous basis). Reference analyses are the same as in Figure 7.
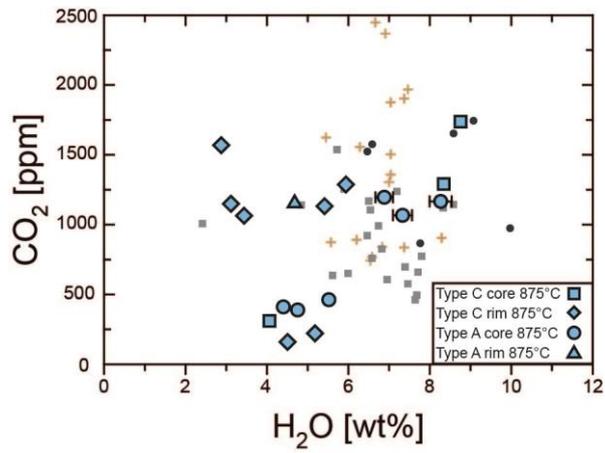
94

95

96 **FIGURE 9** H_2O and CO_2 content measured in remelted nanogranitoid inclusions. Error bars

97 are displayed only when bigger than the symbol. Data for MI from the Ivrea Zone (Carvalho

98 et al. 2019) are also reported for comparison (black dots = upper amphibolite facies, grey

99 squares = transition zone, brown crosses = granulite facies).

100

101

102

103

104

105

106

107

108

109

110

111
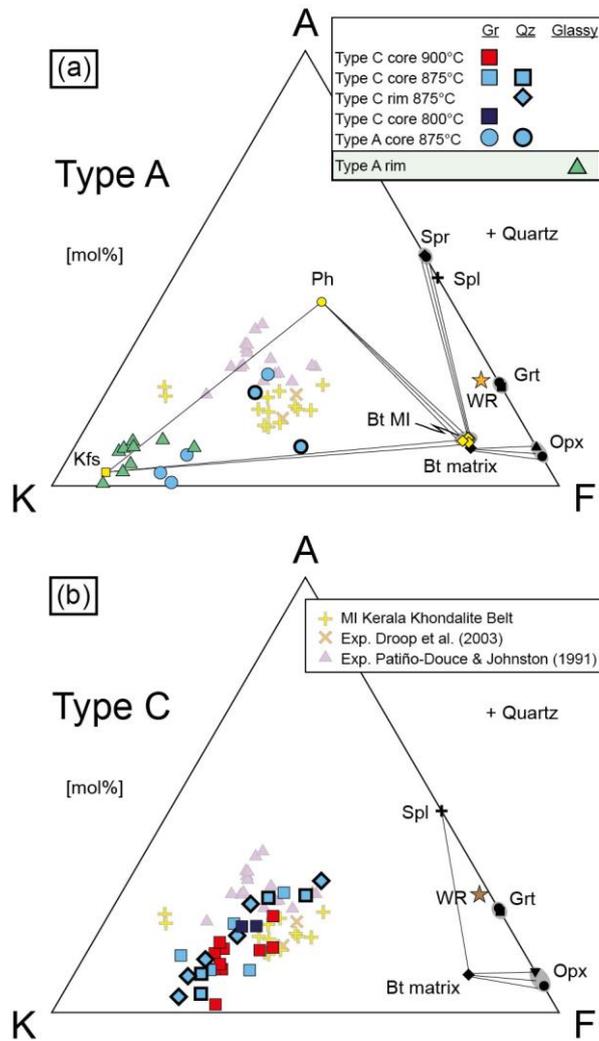
FIGURE 10 AKF diagram (after Vielzeuf & Holloway,1988) projected from quartz for MI

and bulk rocks. (a) Type A granulite. (b) Type C granulite. Also reported for comparison are:

melt inclusions from the Kerala Khondalite Belt (Cesare et al. 2009; Ferrero et al. 2012),

experimental glasses (900 °C, 5 kbar) of Droop et al. (2003) and experimental glasses (875-

1075 °C, 7-13 kbar) of Patiño-Douce & Johnston (1991).

117

118

119

120

121

122

**FIGURES FOR THE ELECTRONIC APPENDIX**
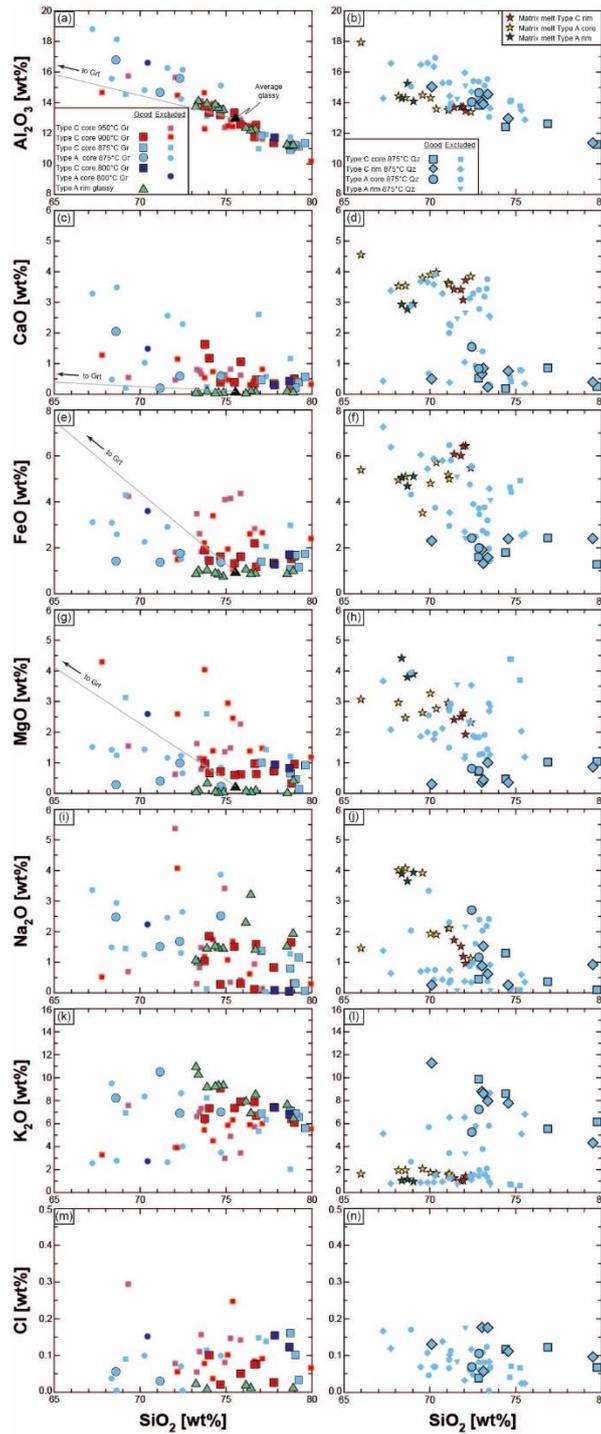
124

125 **FIGURE S1** Harker diagrams showing the complete set of MI analyses. Small symbols

126 represent disregarded analyses. The line displayed for Al_2O_3, FeO and and MgO represents

127 the tie-line between the host garnet (Type A granulite) and the average composition of the

128 glassy inclusions (black triangle).

129

130
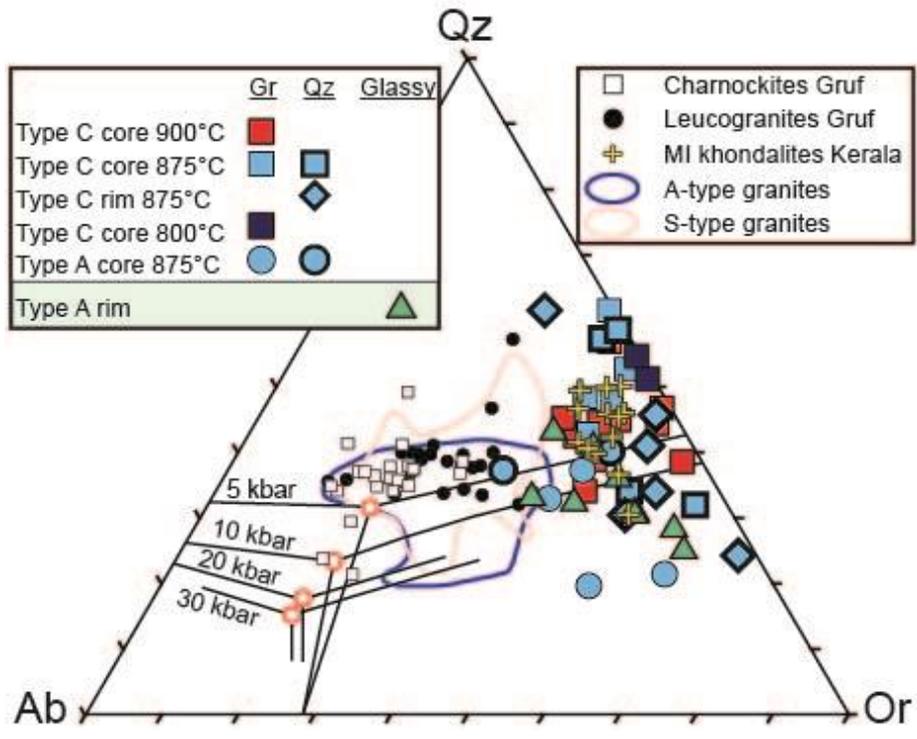
131

132

133 **FIGURE S2** CIPW Qz-Ab-Or diagram showing normative compositions for the analysed MI
134 and other reference analyses from the literature (see text).

135

136

137
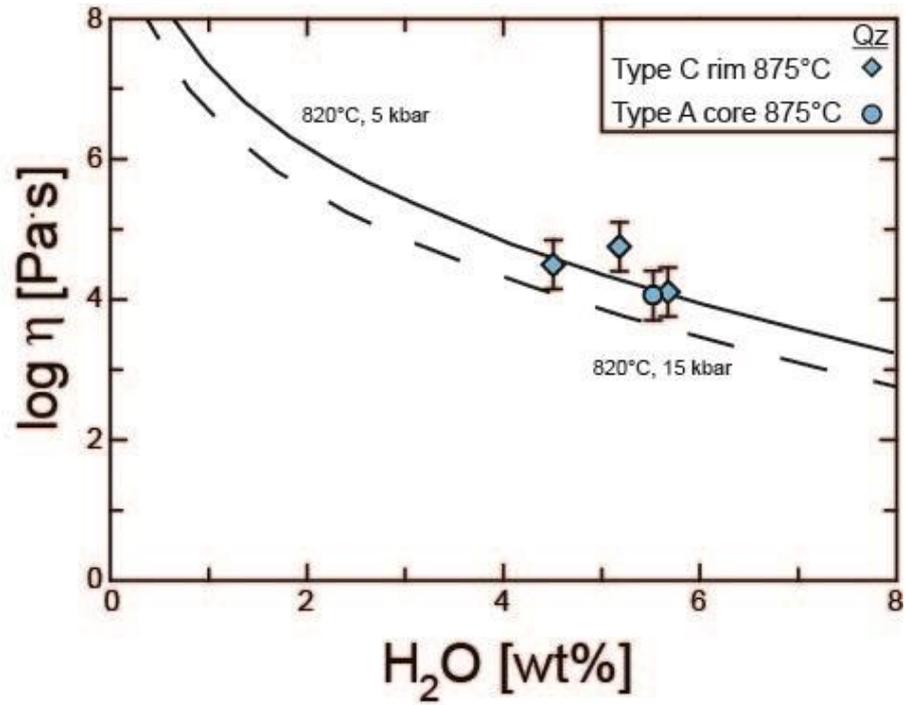
FIGURE S3 Viscosities of rhyolitic melts vs. H_2O content (modified after Ardia et al., 2008). Viscosities for MI are calculated according to Giordano et al. (2008).